Titre: Title:	Comparison of Myelin Imaging Techniques in Ex Vivo Spinal Cord
Auteur: Author:	Manh Tung Vuong
Date:	2017
Type:	Mémoire ou thèse / Dissertation or Thesis
Référence: Citation:	Vuong, M. T. (2017). Comparison of Myelin Imaging Techniques in Ex Vivo Spinal Cord [Master's thesis, École Polytechnique de Montréal]. PolyPublie. https://publications.polymtl.ca/2683/

UNIVERSITÉ DE MONTRÉAL

COMPARISON OF MYELIN IMAGING TECHNIQUES IN EX VIVO SPINAL CORD

MANH TUNG VUONG

INSTITUT DE GÉNIE BIOMÉDICAL

ÉCOLE POLYTECHNIQUE DE MONTRÉAL

MÉMOIRE PRÉSENTÉ EN VUE DE L'OBTENTION

DU DIPLÔME DE MAÎTRISE ÈS SCIENCES APPLIQUÉES

(GÉNIE BIOMÉDICAL)

JUILLET 2017

UNIVERSITÉ DE MONTRÉAL

ÉCOLE POLYTECHNIQUE DE MONTRÉAL

Ce mémoire intitulé:

COMPARISON OF MYELIN IMAGING TECHNIQUES IN EX VIVO SPINAL CORD

présenté par : VUONG Manh Tung

en vue de l'obtention du diplôme de : Maîtrise ès sciences appliquées

a été dûment accepté par le jury d'examen constitué de :

Mme PÉRIÉ-CURNIER Delphine, Doctorat, présidente

M. STIKOV Nikola, Ph. D., membre et directeur de recherche

M. COHEN-ADAD Julien, Ph. D., membre et codirecteur de recherche

M. POULIOT Philippe, Ph. D., membre

DEDICATION

To my beloved family, Tinh, Minh, Tuan, Ha, Khoi and My!

ACKNOWLEDGEMENTS

"Your work is going to fill a large part of your life, and the only way to be truly satisfied is to do what you believe is great work. And the only way to do great work is to love what you do. If you haven't found it yet, keep looking. Don't settle."

This quote, which is excerpted from the commencement address delivered by Steve Jobs at Stanford university in 2005, has inspired me a great deal to change my career path from information and communication technology to a research project related to healthcare or health science. In the summer of 2015, I started my Master's project at the NeuroImaging Research Laboratory (NeuroPoly) of École Polytechnique, Université de Montréal, under the mentorship of of Professors Nikola Stikov and Julien Cohen-Adad.

Professor Nikola Stikov was my supervisor and I would never have been able to finish my thesis without his excellent advice and guidance. He has such an enormous energy to spread that people around could feel his passion and get inspired immediately. Nikola always tries to walk in the students' shoes to give them freedom and confidence but at the same time provide very rigorous guidance to help students improve from a little thing to the whole picture. I would never forget the tremendous efforts he made, literally worked day and night to correct my scholarship documents, our scientific abstracts and this thesis. I owe this Master's degree to him.

I would like to express my great appreciation to Professor Julien Cohen-Adad who was my co-supervisor and also the first person that led me to this field. He always encourages students to ask questions, discuss topics in great detail and therefore develop the critical thinking skills. Julien provided many instant solutions to my scientific and non-scientific problems that I encountered during my time at Neuropoly. I am really impressed and inspired by his passion and perspective of work in research.

Tanguy Duval was a PhD student and helped me understand many concepts regarding MRI with hands-on experiences. He shared a great deal of time with me for scanning acquisitions and data processing. Tanguy has an excellent multi-tasking skill that allows him to cover a bunch of topics from MRI to histology. I am blessed to have him as a collaborator and a friend to share too many unforgettable memories throughout this journey.

I would like to thank Ariane Saliani, for her help in preparing the samples and doing histology for our MRI validation. I know that takes a lot of work and careful attentions. I am also grateful to Aldo Zaimi who provided instant supports to me regarding axon segmentation. I thank both of them for many jokes we laughed during lunchtime and for running with me before the deadlines.

I thank Ian Gagnon and Tanguy for translating the abstract into French and helping me with the data documentation.

And there, other colleagues at NeuroPoly, thanks to Grégoire Germain, Tommy Boshkovski, Gabriel Mangeat, Benjamin De Leener, Ryan Topfer, Sarah Dupont, Simon Levy, Alexandru Foias, Nibardo Lopez Rios, Agah Karakuzu, Atef Badji, Charley Gros, Darya Morozov, Pascale Beliveau and all others for the excellent working environment at Neuropoly and for the unforgettable time there as well as at the conferences in Singapore and Hawai'i.

I am particularly indebted to my parents, Vuong Van Tinh and Nguyen Thi Minh, my brother and sister-in-law, Vuong Quoc Tuan and Nguyen Thi Ha, my nephew, Vuong Tuan Khoi and my recently-born niece, Vuong Ha My, for their infinite love, encouragement and inspiration during my time in Italy and now in Canada, exactly halfway around the world apart. I dedicate this thesis to them, my beloved family.

Many thanks to Richard, the best roommate ever, for his encouragement and cooking for me when I was running with the deadlines. I owe him for showing me the Québécoise culture and teaching me French.

I thank my best Vietnamese friends in Montreal, Tuong Hoang and Hieu Nguyen, for their supports during my arrival in Montreal and for helping me treat my homesickness.

I would like to thank Mark Does and Kevin Harkins from Vanderbilt University, Eva Alonso-Ortiz and Ives Levesque from McGill University, Philippe Pouliot, Jean-François Cabana from Polytechnique Montreal for their support during the method implementations and data processing.

Finally, I thank Polytechnique Montreal, NeuroPoly lab, Quebec BioImaging Network for the financial support of my Master's program.

This work was funded by the Canada Research Chair in Quantitative Magnetic Resonance Imaging (JCA), the Canadian Institute of Health Research [CIHR FDN-143263], the Canada Foundation for Innovation [32454], the Fonds de Recherche du Québec – Santé [28826], the Fonds de Recherche du Québec - Nature et Technologies [2015-PR-182754], the Natural Sciences and Engineering Research Council of Canada [435897-2013, 06774-2016] and the Quebec BioImaging Network.

Manh-Tung Vuong

École Polytechnique, Université de Montréal

June 19, 2017

RÉSUMÉ

La myéline est un matériau diélectrique qui entoure l'axone des neurones, et qui permet une transmission plus rapide des influx nerveux. La perte de myéline peut avoir de graves conséquences, allant d'interruptions mineures jusqu'à l'arrêt total de la propagation des influx nerveux dans le cas de maladies neurodégénératives telles la sclérose en plaque et la maladie de Parkinson. Présentement, il existe un débat au sein de la communauté d'imagerie de la myéline à savoir quel biomarqueur basé sur l'imagerie par résonance magnétique (IRM) possède la meilleure corrélation à la myéline.

Dans ce travail, nous comparons plusieurs techniques d'imagerie de la myéline qui sont basées sur l'IRM (quantitative magnetization transfer imaging, myelin water imaging, and proton density imaging) en évaluant leur reproductibilité et leur concordance avec l'histologie haute résolution (<μm) de coupe transversale complète de la moelle épinière d'un rat, d'un chien et d'un humain. Alors qu'il y a des études qui se penchent sur la relation entre deux de ces méthodes et l'histologie, il s'agit, au meilleur de nos connaissances, de la toute première étude qui implémente et compare toutes ces méthodes à la fois dans le but de mieux comprendre les corrélations existant entre elles et à la myéline.

Qualitativement, les contrastes étaient similaires et toutes les techniques possédaient des scan-rescan semblables en plus de corréler avec l'histologie. Étonnamment, les corrélations voxelwise entre les différentes mesures de myéline étaient presque aussi élevées que celles entre les scan-rescan. La corrélation diminue seulement lorsque la matière blanche est considérée, ce qui pourrait être dû à la faible plage dynamique de myéline dans la matière blanche à des effets de pénétration des fixatifs dans les tissus et à des problèmes de focus et de stabilité de la microscopie à grand champ. En somme, nous concluons que les différentes techniques d'imagerie de la myéline explorées dans cette thèse possèdent une sensibilité à la myéline semblable. La corrélation avec l'histologie suggère que davantage de travail serait nécessaire pour déterminer le protocole optimal d'imagerie de la myéline.

Cette étude a aussi mis en évidence des problèmes de calibration des mesures IRM. Ainsi que des problèmes de traitement de données qui ont impacté l'exactitude des mesures. Par exemple la mesure de la carte B_1, des problèmes de spoiling ainsi que la variation des délais. Nous avons ainsi standardisé le traitement des données avec le développement de qMRILab qui

intègre en plus des méthodes qMT, méthodes de mapping T_1 et de cartes de champs. De plus, les données de la moelle épinière de chien présentées dans cette étude seront publiées en open source pour que n'importe qui puisse reproduire et tester ces méthodes et d'autres.

ABSTRACT

Myelin is a dielectric material that wraps around the axons of nerve fibers to enable fast conduction of signals throughout the nervous system. Loss of myelin can cause anywhere from minor interruption to complete disruption of nerve impulses in a range of neurodegenerative diseases such as multiple sclerosis and Parkinson's disease. There is an ongoing debate in the myelin imaging community about which biomarker based on Magnetic Resonance Imaging (MRI) is more correlated with myelin.

In this work, we implemented and compared several MRI-based myelin imaging techniques (quantitative magnetization transfer imaging, myelin water imaging, and proton density imaging) by evaluating their repeatability and their relation to large-scale histology in the ex vivo spinal cords of a rat, a dog, and a human. While there are studies investigating the relationship between pairs of them as well as with histology, to the best of our knowledge, this is the first study that implemented and compared all those methods at the same time to evaluate their reproducibility and their correlation with myelin.

Qualitatively the contrasts were similar, and all techniques had comparable scan-rescan and correlations with histology. Surprisingly, the voxel-wise correlations between the various myelin measures were almost as high as the scan-rescan correlations. The correlations decreased when only white matter was considered, which could be due to the small dynamic range of the measurement, or due to artifacts related to the preparation and panoramic scanning of the tissue. We conclude that the myelin imaging techniques explored in this thesis exhibit similar specificity to myelin, yet the histological correlations suggest that more work is needed to determine the optimal myelin imaging protocol.

The study also pointed out some potential miscalibrations during acquisitions as well as data processing that may lead to anywhere from minor to major impact on the accuracy of the results. These include B_1 mapping, insufficient spoiling and variation of the predelay time. We have also standardized the data processing routines by upgrading qMTLab to qMRLab which adds several quantitative MR methods to the toolbox, such as standard T_1 mapping and field mapping. In addition, the data of the dog spinal cord in this study will be published together with the analysis scripts to help the interested reader to reproduce the findings from this thesis.

TABLE OF CONTENTS

LIST OF TABLES

LIST OF FIGURES

LIST OF SYMBOLS AND ABBREVIATIONS

CNS	Central nervous system
CSF	Cerebrospinal fluid
ESP	Echo spacing time
FID	Free induction decay
GM	Gray matter
IR	Inversion recovery
MRI	Magnetic resonance imaging
MS	Multiple sclerosis
MTR	Magnetization transfer ratio
MTV	Macromolecular tissue volume
MWF	Myelin water fraction
NLS	Nonlinear least-squares
NNLS	Non-negative least squares
PBS	Phosphate-buffered saline
PD	Proton density
PFA	Paraformaldehyde
qMT	Quantitative magnetization transfer
RF	Radio frequency

SIRFSE	Selective inversion recovery fast spin echo
SPGR	Spoiled gradient
SS	Steady state
TE	Echo time
TI	Inversion time
TR	Repetition time
WM	White matter
WSC	Whole spinal cord

CHAPTER 1 INTRODUCTION

According to the Multiple Sclerosis (MS) International Federation, Canada ranks first in the world with nearly 300 cases per 100,000 people [1]. MS is one of the most common neurodegenerative diseases of the central nervous system (CNS), and it is currently classified as an autoimmune disease. Specifically, the immune system attacks myelin, a dielectric sheath that wraps around the nerve fibers and enables fast transmission of signals through the nervous system. Loss of myelin can cause anywhere from minor interruption to complete disruption of nerve impulses due to axonal degeneration. There is an ongoing debate in the myelin imaging community about which biomarker based on Magnetic Resonance Imaging (MRI) is more correlated with myelin.

1.1 The basics of MRI

In 1946, Felix Bloch stated in his Nobel Prize winning paper that the nucleus of an atom behaves like a magnet [2-4]. A charged particle, such as a proton and a neutron, spinning around its own axis generates a magnetic field, similar to a tiny bar magnet with a north and a south pole. Since then, MRI has made significant strides forward.

"The phenomenon of nuclear magnetic resonance arises in atoms with an odd number of protons and/or an odd number of neutrons. These atoms possess a property known as spin angular momentum [5]." The spin angular momentum ($S = \hbar I$) is a vector proportional to **I**, the spin operator in quantum mechanics, with a proportionality factor defined by Planck's constant ($\hbar$).

The main principles behind MRI are described by the resonance equation ($\omega=\gamma B$), which shows that the resonance frequency of a spin (ω), called the Larmor frequency, is proportional to the magnetic field (B) which the spin is experiencing by a factor (γ) called the gyromagnetic ratio, a known constant unique for each nuclear species. The gyromagnetic ratio for hydrogen is $\gamma/2\pi$= 42.577 MHz/T compared to $\gamma/2\pi$= 10.7 MHz/T for ^{13}C. Associated with the spin angular momentum **S**, a magnetic dipole moment μ is defined as $\boldsymbol{\mu}=\gamma\mathbf{S}$. The MR signal comes primarily from the hydrogen atoms which contains a single proton, and these atoms are used to reconstruct images. There are two reasons to use hydrogen. First, the body consists of largely water and fat, both of which are rich in hydrogen. Second, the gyromagnetic ratio for hydrogen is the largest, hence the hydrogen Larmor frequency is the most sensitive to changes in the magnetic field [5].

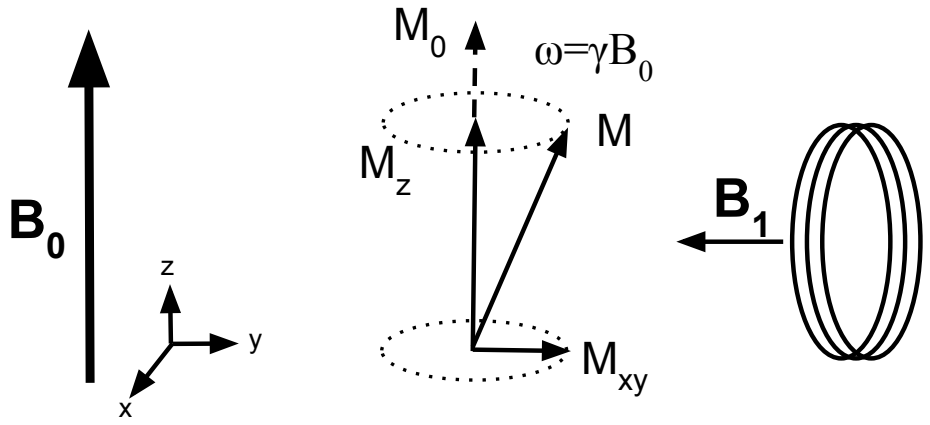

Figure 1.1: MR basics using classical physics (adapted from [6])

MRI is based on the interactions of spins with the main field B_0, the radio frequency field B_1, and the linear gradient fields G. In the presence of the main field B_0 (usually on the order of several Tesla), a magnetization moment **M** is produced in the direction of this field and nuclear spins exhibit resonance at the Larmor frequency, as shown in Figure 1.1. In classical physics, the magnetization moment can be described as $\mathbf{M}=\sum\boldsymbol{\mu}$. The net magnetization will be excited by a radio-frequency (RF) field tuned to the Larmor frequency. The RF field is applied in the transverse plane, which rotates the magnetization vector by a certain angle, called the tip angle, flip angle or rotation angle. The tipped vectors will precess in the transverse plane at the Larmor frequency after the RF field is turned off. As the excited protons try to get back to their low energy states, a process of relaxation occurs. T_1 relaxation describes what happens to the magnetization along the longitudinal axis. The net magnetization will re-grow along the z-axis. Relaxation in the transverse plane (called T_2 relaxation), happens simultaneously with T_1 relaxation. The transverse relaxation is caused by the fact that the magnetization vectors start to dephase after the RF field is turned off. Imagine an analogy where the spins are children in a class under the supervision of a teacher (the B_1 field). During class the teacher keeps the students in order, so they are all in phase, sitting at their desks. When the class is over (RF is turned off), they run out of the classroom and each one has a different pace, so dephasing occurs.

The dynamics of the nuclear magnetization can be described by the Bloch equation:

$$\frac{dM}{dt} = M \times \gamma B - \frac{M_x i + M_y j}{T_2} - \frac{(M_z - M_0)k}{T_1} \tag{1.1}$$

where γ is the gyromagnetic ratio, T_1 is the longitudinal-z relaxation time constant, T_2 is the transverse-xy relaxation time constant, M_0 is the equilibrium sample magnetization due to B_0 field; i, j, k are the units vectors in x, y, z directions respectively.

The generated time signal received at an RF receiver coil during relaxation is called free induction decay (FID). However, with this setup, there is no way to localize the spins, as the signal is generated from all spins in the excited region. Therefore, it is not possible to differentiate the signals from spins at different spatial locations. To get spatial localization, it is customary to use so-called linear gradient fields. Due to the specific roles that the gradients play, the gradients applied along the x-axis, y-axis, z-axis are often referred to as the readout gradient, the phase-encoding gradient, and the slice-selection gradient, respectively

1.2 Conventional MRI

Conventional MRI is not capable of directly measuring myelin. This is because myelin is composed of approximately 80% lipid and 20% protein [7], so it has a very short transverse relaxation time T_2, which is on the order of microseconds. In other words, the signal from myelin decays so fast that the scanner does not have enough time to manipulate and capture the signal due to certain hardware restrictions such as gradient slew-rate. Moreover, it might not be possible to differentiate the signal contribution from protons bounds to macromolecules in myelin from other nonaqueous tissues in the central nervous system [8]. One well-known approach for directly measuring myelin is ultrashort echo time (UTE) imaging [9]. The challenge of this method comes from the contaminating signal from water, which has a long transverse relaxation time T_2, on the order of seconds. Some recent results [10] showed the potential of this technique; however, the issue of water contamination needs to be addressed, before UTE can be considered in the context of clinical MRI. As UTE is still not ideal for direct measurement of myelin content, we need to resort to indirect approaches to quantifying myelin.

Some conventional indirect myelin imaging techniques show high sensitivity, but relatively low specificity to myelin. Two of them are T_1-weighted and T_2-weighted imaging, both of which have been used extensively in clinical MRI. However, these techniques assume that

myelin is the only nonaqueous tissue associated with myelination, which is rarely the case, especially when considering neurodegenerative processes [8].

1.3 Quantitative MRI of myelin

"Quantitative MRI (qMRI) aims at providing values that are intrinsic to the tissue properties. qMRI has the advantage of providing absolute and normative values that could be used for diagnosis, prognosis, multiple-site studies, and ultimately clinical trials [11]." The quantitative approaches to myelin imaging are expected to be more sensitive and more specific to biological changes in the tissues, therefore can provide more insights into the pathogenesis of demyelinating diseases such as MS. Some potential quantitative biomarkers in the efforts to quantify myelin indirectly include the pool size ratio, or bound pool fraction (F, obtained from quantitative magnetization transfer imaging [12, 13]), the myelin water fraction (MWF, obtained from multi-exponential T_2 fitting [14]) and the macromolecular tissue volume (MTV, obtained from proton density imaging [15]). In the literature, low correlations were found between MRI-based metrics of myelin. For example, Sled et al. [16] showed a negative correlation between F and MWF, Dula et al. [17] showed a correlation of 0.18 between F and MWF, and Mezer et al. [15] found a correlation of 0.3 between MTV and F. Regarding the correlation of these metrics with histology, a study in rat spinal cord by Dula et al. [17] did not find positive correlation between F and MWF with histology. A low correlation was also observed between MTV and histological metrics in a cat spinal cord model by Duval et al [18].

Each method has their own advantages and disadvantages depending on which factors we are considering. For example, in terms of implementation, proton density imaging may be easy to implement due to the simplicity of acquisition and the availability of the standard sequences on the scanners, but its metric, MTV, may be sensitive to macromolecules other than myelin and is particularly blind to microanatomic variation between white matter tracts. On the other hand, qMT using the SIR-FSE sequence needs some customization of the standard fast spin echo sequence. In addition, this method does not allow multi-slice imaging and the scan times are long. Myelin water imaging may require shorter echo spacing to take signals from shorter T_2 components into account; and this may not always available to all scanners and may require some sequence customization as well. Data processing for qMT using the SPGR sequence is more

complicated due to the additional maps for correction. More insights into those methods and a comparison between them will be presented in the next chapters.

The objectives of this thesis are (i) to develop a framework for comparing myelin imaging methods and (ii) to implement and compare four MR-based myelin imaging techniques by evaluating their repeatability and their relation to large-scale histology in the ex vivo spinal cords of a rat, a dog, and a human. While there have been studies doing pairwise comparisons and histological validation of the above techniques, to the best of our knowledge this is the first study that implemented and compared all those methods at the same time and looked into their reproducibility and their correlation with other myelin metrics. Chapter 2 will outline the methods used. Chapter 3 will present the comparison of these methods in ex vivo dog, rat and human spinal cord. Finally, Chapter 4 will conclude and put the work in perspective. The appendix entitled ‘Documentation’ explains the details of the data analysis and can be used to replicate this study.

CHAPTER 2 LITERATURE REVIEW

2.1 Myelin

2.1.1 Myelin structure

Myelin is a dielectric material that wraps around the axons of nerve fibers to enable fast conduction of signals throughout the nervous system. Myelin makes up approximately 50% of the dry weight of white matter, giving it its distinctive color [8].

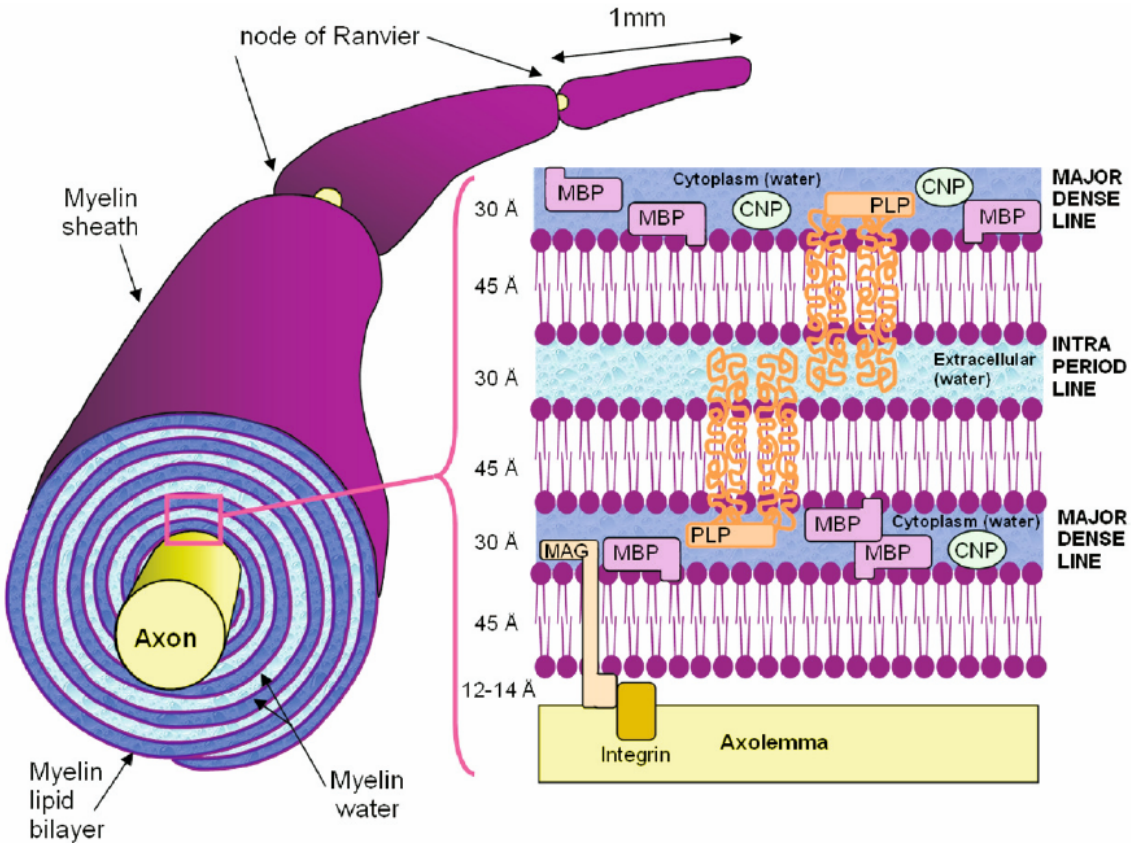

Figure 2.1: Myelin structure [8].

As stated in a recent review by Laule and colleagues, "myelin is produced by oligodendrocytes and is comprised of tightly compacted oligodendrocyte cell membranes, which are wrapped around the axon in a concentric lamellar fashion (Figure 2.1)." Oligodendrocyte produce large amounts of myelin, approximately 5000 mm^2 to 50,000 mm^2 of myelin surface area per cell per day. This does not happen throughout the lifetime, but only during periods of

active myelin assembly. Along the axon there are unmyelinated loci, called the nodes of Ranvier. [8].

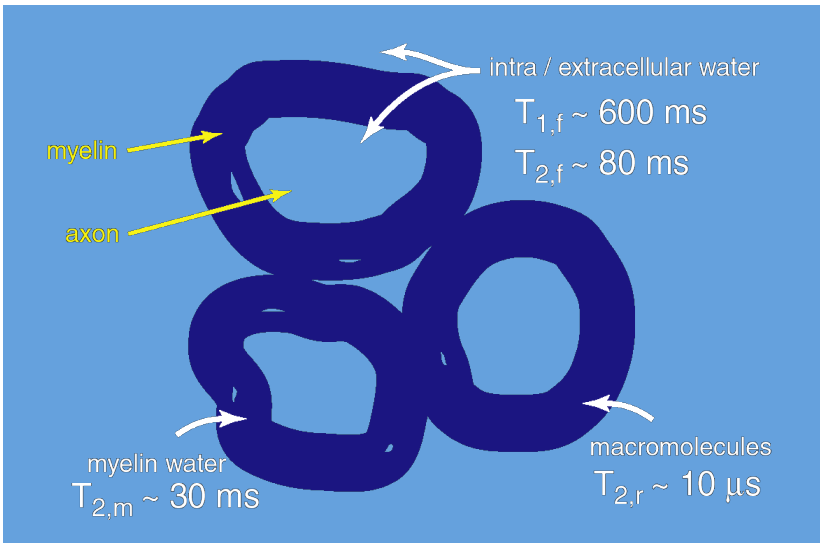

Figure 2.2: The relaxation times in myelin tissue. The intra- and extra-cellular water have relatively long T_1 and T_2, unlike the water trapped in the myelin sheaths. The T2 of the macromolecules is orders of magnitude smaller. (Image courtesy of Bruce Pike)

“ The myelin bilayer is made of approximately 80% lipid and 20% protein. The intracellular and extracellular space in between the bilayers is filled with water, which makes up approximately 40% of the weight of myelin [8].”

Figure 2.2 shows the relation between myelin structures and their respective relaxation times. The intra- and extra-cellular water have relatively long T_1 and T_2, unlike the water trapped in the myelin sheaths. The T_2 of the macromolecules is orders of magnitude smaller.

2.1.2 Myelin function

Myelin is like an electrical insulator. Just like plastic wrapped around a copper wire, it significantly increases the the speed of action potential transmission. In the white matter, this increase in speed is somewhere between 10 and 100 times compared to an unmyelinated axon. One parameter that is very important to conduction speed is the g-ratio, defined as the ratio of the inner to the outer radius of the myelin sheath. Lower g-ratio (thicker myelin) is observed in the central nervous system, compared to peripheral nerves [19]. It is because of myelin that “saltatory

conduction of the action potential is much faster than the continuous conduction by sodium channels evenly distributed along the unmyelinated axon" [8].

There is a very tight coupling between the myelin and the axon, and damage to one is often accompanied by damage to the other. Therefore, axon and myelin content are highly correlated, and it is difficult to decouple the two.

2.2 Proton density imaging

Macromolecular tissue volume (MTV) is a fundamental measure of brain anatomy that represents the fraction of a voxel filled with brain tissue (non-water), which is complemented by the water volume [15]. The voxel water volume is estimated from the proton density (PD) signal. PD represents the concentration of mobile hydrogen atoms in tissues and is proportional to the water volume. This constant of proportionality is determined by normalizing with respect to the cerebrospinal fluid (CSF) that is considered to be 100% water [15]. Therefore, water volume fraction (WVF) is measured as the normalized PD in each voxel and has a value between 0 and 1. The voxel MTV fraction (MTVF) is defined as the complementary fraction of MVF (MTVF = 1 – WVF).

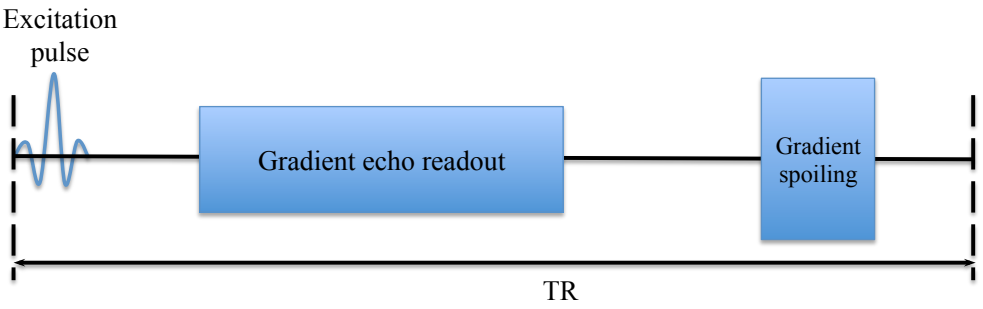

Figure 2.3: Spoiled gradient echo (SPGR) sequence.

The method utilizes a spoiled gradient echo (SPGR) sequence (Figure 2.3), where the transverse magnetization is destroyed after each repetition time TR by RF spoilers and gradient spoilers. This is a steady-state (SS) sequence which means the whole sequence is repeated until SS is achieved and that data is only acquired when SS is reached, which might take about 200 repetitions [20]. The SPGR signal for a flip angle α is written as follows [15]:

$$S(\alpha) = M_0 \sin(\alpha) \frac{1 - e^{\frac{-TR}{T_1}}}{1 - \cos(\alpha) e^{\frac{-TR}{T_1}}} \tag{2.1}$$

where M_0 incorporates g, a scale factor that characterizes receive-coil inhomogeneity gain, PD and T_2^* effects (T_2^* relaxation contribution is assumed to be negligible due to the relatively short TE):

$$M_0 = g \times PD \times e^{\frac{-TE}{T_2^*}} \approx g \times PD \tag{2.2}$$

As the non-linear fitting for equation (2.1) is slow, linearization can be performed as follows:

$$\frac{S(\alpha)}{\sin(\alpha)} = A \frac{S(\alpha)}{\tan(\alpha)} + B \tag{2.3}$$

where:

$$A = e^{\frac{-TR}{T_1}} \tag{2.4}$$

$$B = M_0 (1 - e^{\frac{-TR}{T_1}}) = M_0 (1 - A) \tag{2.5}$$

At least two different flip angles are required for the linear fitting procedure derived from SPGR imaging. The fitting produces a T_1 map and an M_0 map. In practice, transmit-coil and receive-coil imperfections can lead to bias because (i) the transmit-coil inhomogeneity can affect the flip angle and (ii) the receive-coil inhomogeneity can influence the M_0 term.

The flip angles can be corrected by using a separate B_1^+ field map, defined as the ratio of the actual flip angle to the nominal flip angle. There is a wide range of techniques to derive a B_1^+ field map. Depending on whether the magnitude or phase of the images is used, most methods can be classified into two categories: magnitude-based methods (such as the double-angle method [21] or actual flip angle method [22]) and phase-based methods (such as Bloch-Siegert shift method [23]). The double-angle method is the most popular method in a two-dimensional experiments due to its ease of implementation. The method requires two acquisitions with two nominal flip angles of α and 2α. The signal magnitudes can be written as follows:

$$S_{\alpha} = A\sin(\alpha) \tag{2.6}$$

$$S_{2\alpha} = A\sin(2\alpha) = 2A\sin(\alpha)\cos(\alpha) \tag{2.7}$$

where A is the magnitude of the equilibrium magnetization. As a results, the actual flip angle (α_{act}) and the B_1^+ map can be estimated by:

$$\alpha_{act} = \arccos(\frac{S_{2\alpha}}{2S_{\alpha}}) \tag{2.8}$$

$$B_1^+ = \frac{\alpha_{act}}{\alpha} \tag{2.9}$$

After smoothing the B_1^+ map using local regressions of hyperplanes (3D) [15], high-resolution T_1 map and M_0 map are calculated using SPGR images with a linear fitting based on equation (2.3) or nonlinear least-squares (NLS) fitting based on equation (2.1). The latter is more complex and slower but can minimize the difference between the data and the signal equation predictions [15].

The flip angles can also be corrected by combining SPGR images with gold-standard T_1 maps derived from an inversion recovery (IR) sequence, thus removing the effects of transmit-coil inhomogeneity [24, 25]. Figure 2.4(top) depicts the inversion recovery sequence that includes two RF pulses (separated by an inversion time TI). One RF pulse inverts the longitudinal magnetization M_z and the other flips the recovered longitudinal magnetization into the transverse plane. They are followed by a spin-echo or gradient-echo readout, which samples the MR signals according to the Bloch equations:

$$\frac{\partial M_z(t)}{\partial t} = \frac{|M_0 - M_z(t)|}{T_1} \tag{2.10}$$

Figure 2.4(bottom) shows the T1 relaxation curve for a simple case where TR >>T1. The curve can be sampled at several TI's and fitted to a single exponential model.

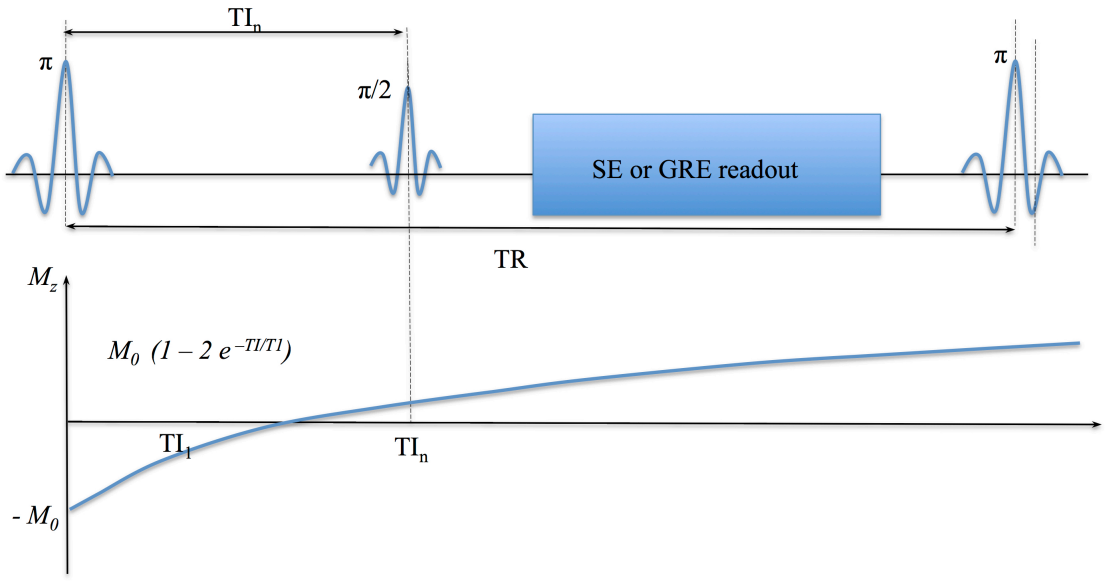

Figure 2.4: A schematic of an inversion recovery sequence (top) and the T_1 recovery curve (bottom) (adapted from [26])

The recently proposed method by Barral et al. [24] standardizes the IR measurements and fits the MR signals to a complex model with five free parameters (a and b are complex numbers, T_1 is real-valued):

$$S_i = a + be^{\frac{-TI_i}{T_1}} \tag{2.11}$$

where S_i is the complex signal at TI_i. Therefore, this protocol can get rid of the mentioned assumptions used in the previous models and can provide a more accurate T_1 map.

PD is derived from M_0 after the receive-coil inhomogeneity map is estimated by combining data acquired from the individual coils [15]. As discussed above, CSF is assumed to be filled entirely with water, therefore the unknown constant of proportionality between water volume and PD can be approximated by the mean value of calculated PD in CSF. The WVF and MTVF can then be derived accordingly.

Because MTV does not only measure myelin, but also glial cell membranes and organelles, MTV needs to be calibrated to obtain the absolute myelin content. Interestingly, a recent study by Duval et al. [27] showed that MTV can be used as a reasonable approximation of absolute myelin

content in healthy tissue without using a proportionality constant. However, this relationship might vary and needs to be tested extensively in pathological white matter.

2.3 Myelin water imaging

Myelin water imaging or multi-exponential T_2 (MET_2) imaging was first proposed by MacKay et al. [14] to study the MRI-visible water related to myelin. While T_2-weighted images are acquired at a single TE, data at multiple TEs are required for quantitative T_2 relaxation studies to result in a T_2 decay curve (Figure 2.5).

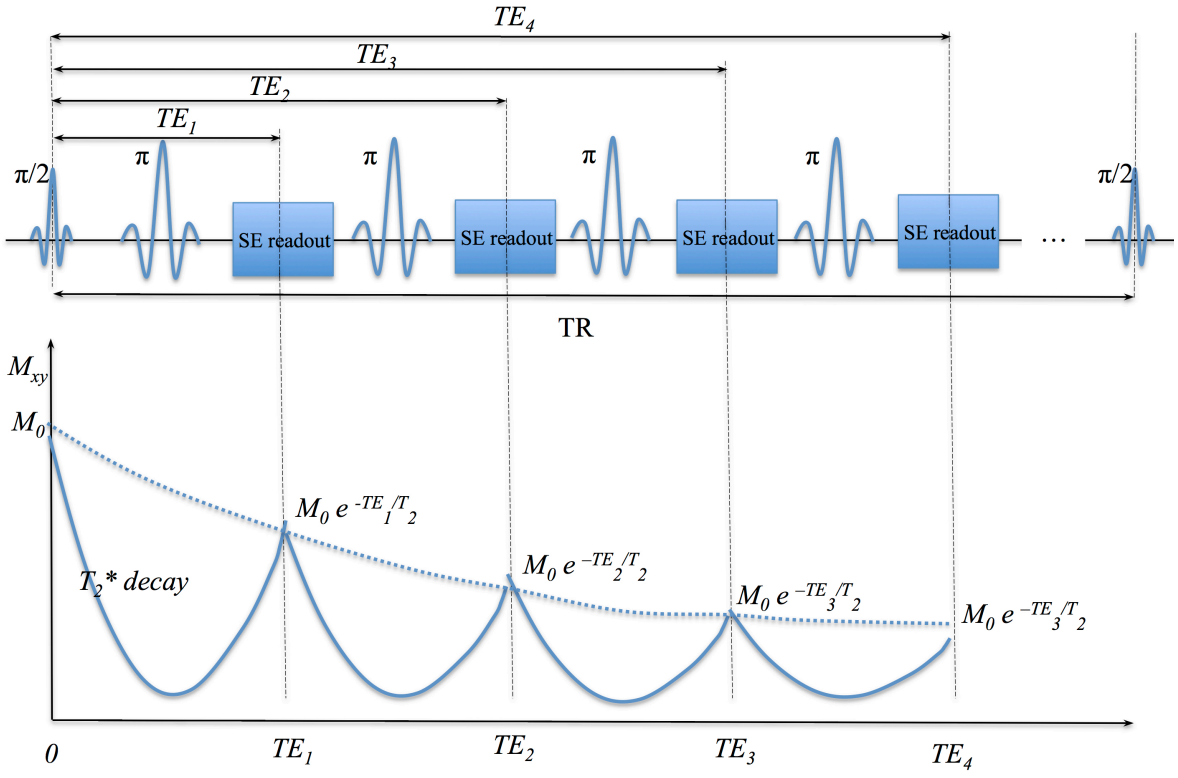

Figure 2.5: A schematic of a multi-echo spin echo sequence (top) and the T_2 decay curve (bottom) (adapted from [26]).

The signal from mobile protons can be classified into different water pools according to their transverse relaxation times. Specifically in the central nervous system they can be separated into three distinguishable compartments [14]: (i) a short T_2 component (10-40ms) which corresponds to water trapped in the myelin sheath, referred to as myelin water, (ii) an intermediate T_2 component (on the order of 80ms) from intra/extra-cellular water, and (iii) a long T_2 component

(on the order of seconds) arising from cerebrospinal fluid (CSF). The third component is usually ignored in the data fitting resulting in a T_2 distribution focusing on the first two components [28]. Figure 2.6 depicts the T_2 distribution.

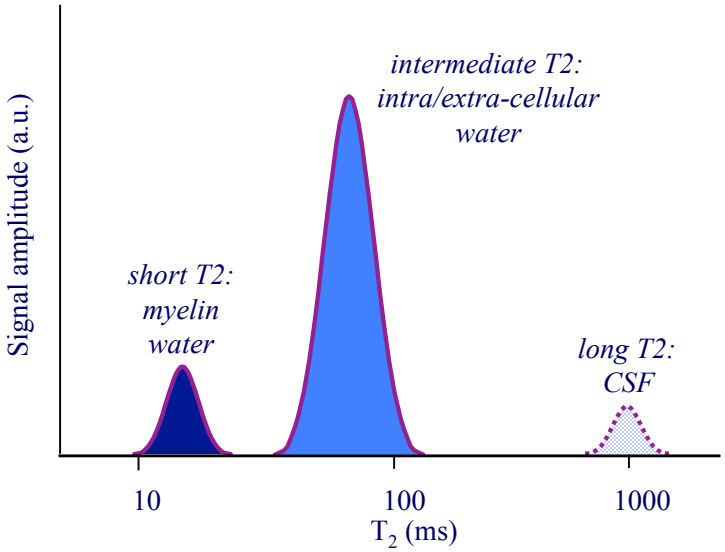

Figure 2.6: Three distinguishable T_2 compartments in the central nervous system (adapted from [14]).

The signal obtained was described in terms of a multi-exponential T_2 decay [14, 28]:

$$y_i = \sum_{j=1}^{M} s_j e^{-t_i/T_{2,j}}, i = 1,2,\ldots,N. \tag{2.12}$$

where N is the total number of data points, y_i, that are measured at times t_i and s_j is the unknown amplitude of the spectral component with a relaxation time $T_{2;j}$. M is the number of logarithmically spaced T_2 times within an appropriately selected range.

The myelin water fraction (MWF) is defined as the fraction of the signal contributions from the first T_2 component (myelin water) to the total signal in the T_2 distribution. In terms of data analysis, extracting the myelin water signal from the multi-exponential relaxation signal can be challenging. The most frequently used approach is non-negative least squares (NNLS) that minimizes a χ^2 misfit and an energy constraint [7, 8]. The energy constraint is used to smooth the T_2 distribution, because minimizing only for χ^2 will create discrete spikes. The following expression is minimized:

$$\chi^2 + \mu \sum_{j=1}^{M} s_j^2, \quad \mu \geq 0 \tag{2.13}$$

with the energy constraint of $1.02\chi^2_{\min} \leq \chi^2 \leq 1.025\chi^2_{\min}$, where $\chi^2_{\min}$ is the result for the case of $\mu = 0$ [7].

Another approach is to linearly combine multiecho data and then filter out the short T_2 component. By using this approach, Vidarsson et al. [29] proposed a three-echo linear combination myelin imaging approach that significantly reduces acquisition time. However, this approach is challenged by the accuracy of short T_2 estimates when only three echoes are used.

2.4 Quantitative magnetization transfer (qMT) imaging

In typical magnetic resonance imaging (MRI), the detected signal comes only from the highly mobile protons in free water, which have sufficiently long transverse relaxation times ($T_2 > 10$ ms) so that acquisition sequences can be run before the signal has completely decayed [30]. The highly mobile protons are referred to as the free pool. In addition, there are also less mobile protons bound to macromolecules such as proteins, lipids and sugars, which have very short transverse relaxation times ($T_2 \approx 10$ μs) and therefore these protons cannot be imaged directly using MRI. They are referred to as the bound pool, the macromolecules pool, or restricted pool.

Due to its very short transverse relaxation time T_2, the frequency spectrum of the bound pool is very broad. On the other hand, free water protons have very narrow absorption lineshapes in the frequency domain due to their long transverse relaxation time. The frequency spectrum or the absorption lineshape is inversely proportional to the transverse relaxation time, and it explains how different RF frequencies affect the magnetization. In general, the hydrogen bound to macromolecules has a broader lineshape (shorter T_2), so it is much more sensitive to off-resonance irradiations. Therefore, the bound pool can be manipulated without perturbing the free pool by applying an appropriately placed off-resonance RF pulse. After the pulse is turned off, this saturation can be transferred to the free pool through a phenomenon called magnetization transfer (MT), causing a decrease in the free water signal.

MT ratio (MTR) is the most common metric quantifying that attenuation and is defined as the relative change in intensity of images acquired without and with off-resonance RF pulses

[30]. A great deal of studies showed a high sensitivity of MTR to tissue damage but this metric is influenced by the overall water and macromolecule content in tissues, as well as other processes such as inflammation and axonal loss [31]. Furthermore, MTR is very sensitive to the pulse sequence parameters and B_0 and B_1 inhomogeneities.

Quantitative magnetization transfer (qMT) on the other hand attempts to remove the effects that plague MTR, providing metrics that are independent of the MRI protocol. Most qMT methods are based on a two-pool model that is simple enough to be analytically tractable and yet sufficient for quantitative interpretation of MT. Figure 2.7 shows a representation of this model in the absence of an applied RF wave, i.e. in free precession. Subscript *f* represents the free pool and subscript *r* corresponds to the restricted pool. Each pool is divided in two groups, representing the state of magnetization: protons that are longitudinally aligned (unshaded) and transverse or saturated magnetization (shaded). The longitudinal magnetization at time *t* for the free and restricted pool respectively is given by $M_{zf}(t)$ and $M_{zr}(t)$, with equilibrium values of M_{0f} and M_{0r}. For each pool, there is a longitudinal relaxation rate, R_{1f} ($=1/T_{1f}$) and R_{1r} ($=1/T_{1r}$) in the absence of magnetization transfer. The rate of magnetization transfer from the free to the restricted pool is denoted k_{fr}, while the rate in the other direction is k_{rf}. The ratio of these rates is related to the ratio of the sizes of the restricted and free water proton pools: $k_{fr}/k_{rf} = M_{0r}/M_{0f} \equiv F$, where F is defined as the pool size ratio.

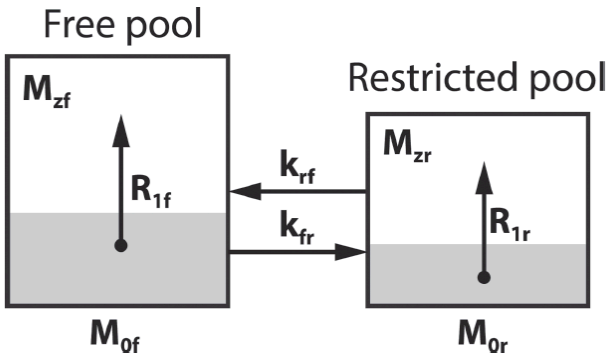

Figure 2.7: Two-pool model of magnetization transfer exchange in the absence of applied radio-frequency pulses (adapted from Henkelman [20, 32]).

As mentioned above, qMT tries to remove the sensitivity of MTR to the sequence parameters. Additionally, it tries to decouple the various contributions to MTR, such as the longitudinal relaxation time T_1, the rate of MT exchange between two pools, and the pool size

ratio, as first proposed by Henkelman et al. [32]. The coupled Bloch equations to model MT exchange for the two-pool system can be written as follows [20, 32, 33]:

$$\frac{\partial M_{xf}}{\partial t} = -\frac{M_{xf}}{T_{2f}} - 2\pi\Delta M_{yf} \tag{2.14}$$

$$\frac{\partial M_{yf}}{\partial t} = -\frac{M_{xf}}{T_{2f}} + 2\pi\Delta M_{xf} - \omega_1(t) M_{zf} \tag{2.15}$$

$$\frac{\partial M_{zf}(t)}{\partial t} = \mathrm{R}_{1f}(M_{0f} - M_{zf}) - k_{fr} M_{zf} + k_{rf} M_{zr} - \omega_1(t) M_{yf} \tag{2.16}$$

$$\frac{\partial M_{zr}(t)}{\partial t} = \mathrm{R}_{1r}(M_{0r} - M_{zr}) + k_{fr} M_{zf} - k_{rf} M_{zr} - W(\Delta, T_{2r}, t) M_{zr} \tag{2.17}$$

where the subscripts *x*, *y*, *z* denote the spatial components of the magnetization vector $\boldsymbol{M}$, $\omega_1(t) = \gamma|B_1(t)|$ is a measure of the RF pulse intensity, γ is the gyromagnetic ratio of the proton and $W(\Delta, T_{2r}, t) = \pi\omega_1^2(t) G(\Delta, T_{2r})$ is the saturation rate of the restricted pool, which depends on its absorption lineshape *G* calculated at different RF frequency offsets (Δ) away from resonance. The lineshape of the free pool can be modeled as a Lorentzian function and the lineshape of the restricted pool is assumed to be a Super-Lorentzian for biological tissues, and a Gaussian for non-biological samples. Figure 2.8 depicts the lineshapes modeled by these functions.

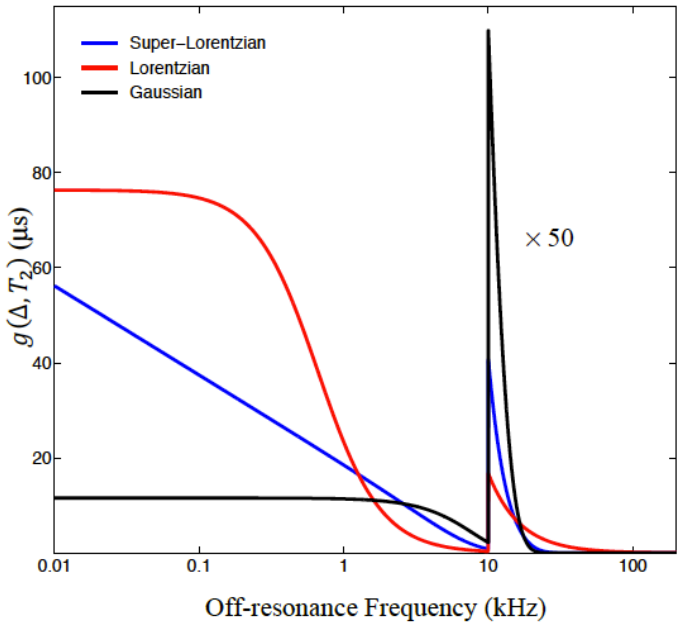

Figure 2.8: Lineshapes modeled by a Super-Lorentzian (T_2=17.7 μs), a Lorentzian (T_2=17.7 μs), and a Gaussian (T_2=29 μs). The lineshapes are 50 times magnified above 10kHz (adapted from [34]).

"The two-pool model is thus characterized by seven parameters: the pool size ratio (F), the exchange rate (either k_r or k_f, the two being related by $F = k_f/k_r$), the longitudinal relaxation rates (R_{1f}, R_{1r}), the transverse relaxation times (T_{2f}, T_{2r}) and the equilibrium magnetization (M_{0f}, with $M_{0r} = F \times M_{0f}$). In general, the set of differential equations (2.14)-(2.17) does not have an analytical solution, except in the simple cases of free precession, when no RF pulse is applied ($\omega_1(t) = 0$, $W(\Delta, T_{2r}, t) = 0$), or when the RF pulse is constant ($\omega_1(t) = \omega_1$ = constant, $W(\Delta, T_{2r}, t) = W(\Delta, T_{2r})$ = constant) [20]. Approximating the pulse sequence by a series of constant amplitude RF pulses (or instant saturations) followed by free precession, allows one to derive an analytical solution and obtain a signal equation that can be fitted to the data. The physical observations of interest are then directly obtained by the fitted parameters. Note that in general, the solutions derived from the Bloch equations cannot distinguish between R_{1f} and R_{1r}. This uncertainty is handled by fixing $R_{1r} = 1\ s^{-1}$ or $R_{1r} = R_{1f}$., with little effect on the fitted parameters [30], thus reducing the number of free parameters to six"[20].

The Henkelman quantitative approach was extended by Sled and Pike [16] using spoiled gradient echo (SPGR) sequences with the presence of off-resonance RF pre-pulses that only

saturate the restricted pool. This approach can be referred to as the off-resonance method. A recent paper proposed saturating the water pool by using a selective inversion recovery fast spin echo (SIRFSE) sequence without utilizing MT off-resonance pulses [13]. This approach is considered an on-resonance qMT method. Regardless of which pulse sequence is used, one of the two pools will be saturated, while leaving the other mostly intact. What happens next is MT between the two pools and we can accordingly measure the pool size ratio based on the corresponding quantitative model.

2.4.1 The qMT off-resonance method (qMT-SPGR)

"MT-SPGR is a Z-spectroscopy imaging method that uses an off-resonance pulsed saturation RF [35]. The basic sequence is represented in Figure 2.9. A shaped RF pulse, of duration t_{mt}, varying power (flip angle α_{mt}) and offset (Δ) is applied to selectively saturate the restricted pool. A delay of time t_s is needed to apply crusher gradients that destroy transverse magnetization, after which an excitation pulse of duration t_p is used before readout. A free precession of time t_r allows the magnetization to recover. This whole sequence is repeated, with repetition time $TR = t_{mt} + t_s + t_p + t_r$, until a steady-state is achieved. MT-SPGR data is usually normalized to data acquired with the same sequence, but without the MT saturation pulse. Moreover, a B_1 map for MT pulse power and excitation flip angle correction and a B_0 map for correction of offset frequencies should be acquired" [20]. The B_1 field map can be acquired using the double-angle method discussed in section 2.2. The B_0 field map can be acquired by the dual-echo method using a simple multi-echo sequence [36]. The first image is acquired at echo time TE_1 $(S_1 = M_1 e^{i.2\pi.\Delta f.TE_1})$ and the second image is acquired at echo TE_2 $(S_2 = M_2 e^{i.2\pi.\Delta f.TE_2})$. If $M_{1,2}$ includes relaxation and coil sensitivities and Δf is the frequency offset, then the B_0 field map is calculated as follows:

$$\Delta f = \frac{\arg(S_1^*.S_2)}{2\pi(TE_2 - TE_1)} \tag{2.18}$$

where S_1^* is the complex conjugate of S_1 .

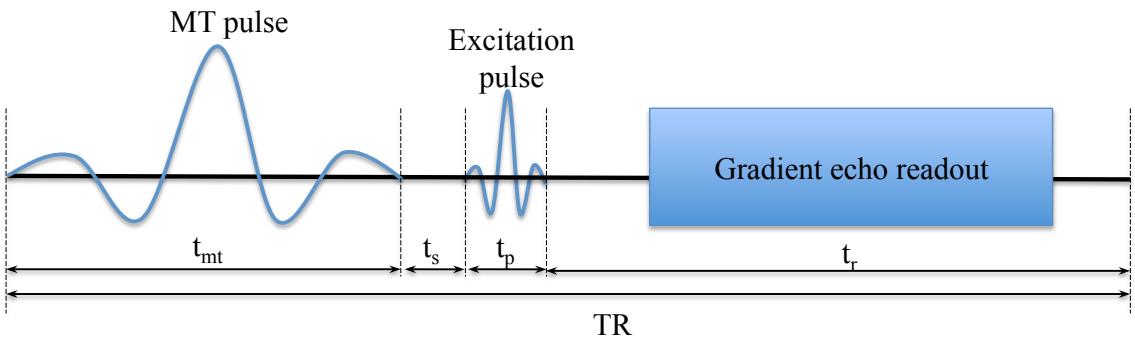

Figure 2.9: SPGR acquisition sequence with MT preparation (adapted from [20]).

"In general, a complementary mono-exponential R_1 map (R_1^{obs}), derived from an inversion recovery T_1 map which was discussed in section 2.2, is also acquired and used to constrain R_{1f} and reduce the number of free parameters [32]:

$$R_{1f} = R_1^{obs} - \frac{k_{fr}(R_{1r} - R_1^{obs})}{R_{1r} - R_1^{obs} + \frac{k_{fr}}{F}} \tag{2.19}$$

By approximating the sequence as a series of constant wave RF, free precession and instantaneous saturation, it is possible to derive an analytical solution to the steady-state signal. The next sub-section will briefly present the Sled and Pike continuous wave (CW) and rectangular pulse (RP) models" [16].

2.4.1.1 Sled and Pike CW

This model describes the SPGR sequence in three steps [37]:

1. Instantaneous saturation of the free pool due to the MT pulse. This effect is given by a saturation fraction, S_f [38]. This fraction is pre-computed in a look-up table by numerical simulation and depends on the MT pulse shape, duration, offset frequency, and amplitude, as well as on T_{2f}.
2. Instantaneous saturation of the free pool by the excitation pulse.
3. A period of continuous wave irradiation of the restricted pool of duration TR. The continuous wave is scaled such that it has equivalent average power as the shaped MT pulse over the duration of the sequence:

$$\omega_{1CW}^2 = \frac{1}{TR} t \int_0^{t_{mt}} \omega_{1mt}^2(t)dt \tag{2.20}$$

Derivation of the analytical solution is given in [16], yielding the normalized signal equation:

$$M_{xy,f} = \frac{(E_1-1)(E_2-1)(\lambda_2-\lambda_1)S_f M_{zf}^{SS}\sin(\alpha)}{(E_1-1)(S_f E_2-1)(\lambda_2-\lambda_1)+(S_f-1)(E_2-E_1)(\lambda_2-R_{1f}-k_f)} \tag{2.21}$$

where $E_1 = e^{-\lambda_1 TR}$, $E_2 = e^{-\lambda_2 TR}$ and

$$\begin{aligned}\lambda_{1,2} = &\frac{1}{2}(R_{1f}+k_{fr}+R_{1r}+k_{rf}+W_r)\pm\ldots \\ &\pm\frac{1}{2}\sqrt{(R_{1f}+k_{fr}+R_{1r}+k_{rf}+W_r)^2-4(R_{1f}R_{1r}+k_{fr}R_{1r}+k_{rf}R_{1f}+R_{1f}W_r+k_{fr}W_r)}\end{aligned} \tag{2.22}$$

$$M_{zf}^{SS} = \frac{M_{0f}(R_{1r}k_{fr}+R_{1r}R_{1f}+R_{1f}k_{rf}+W_r R_{1f})}{R_{1r}k_{fr}+R_{1r}R_{1f}+R_{1f}k_{rf}+W_r R_{1f}+W_r k_{fr}} \tag{2.23}$$

with W_r, the constant RF absorption rates of the restricted pool, given by:

$$W_r = \pi\omega_{1CW}^2 G(\Delta, T_{2r}) \tag{2.24}$$

2.4.1.2 Sled and Pike RP

"The rectangular pulse model [37] uses a similar approach as Sled and Pike CW, but the constant wave MT pulse duration is set equal to the full-width-at-half-maximum (τ_{fwhm}) of the shaped pulse. The equivalent power ω_{1RP}^2 is given by Eq. (2.20), replacing $TR \rightarrow \tau_{fwhm}$, and W_r is given by Eq. (2.24) with $\omega_{1CW} \rightarrow \omega_{1RP}$. This approach does not yield a nice closed-form signal equation, but the result is straightforward to compute in matrix notation." [20].

2.4.2 The qMT on-resonance method (qMT-SIRFSE)

"The method uses a selective inversion recovery (SIR) sequence with short (milliseconds) inversion times. An inversion pulse is applied to selectively invert the free water protons, while only partially saturating the restricted pool. Both pools are allowed to recover for a variable inversion recovery time (t_i), followed by a fast spin echo (FSE) readout and a fixed or variable

delay time (t_d). The signal is fit to a bi-exponential function of t_i and t_d. The sequence is illustrated in Figure 2.10.

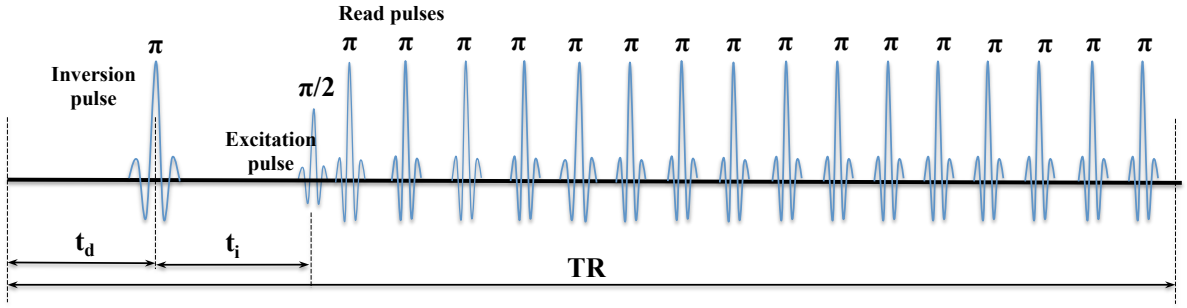

Figure 2.10: SIR-FSE acquisition sequence. t_d is the pre-delay time between acquisitions, t_i is the variable inversion time and TR is the repetition time [13, 20].

Solving the Bloch equations (Equations (2.14)-(2.17)), the evolution of the free water proton signal following a disturbance (when there is no applied RF radiation) is given by a simple bi-exponential:

$$\frac{M_{zf}(t)}{M_{0f}} = b_f^+ \exp(-R_1^+ t) + b_f^- \exp(-R_1^- t) + 1 \tag{2.25}$$

where R_1^- and R_1^+ are the slow and fast recovery rate, with corresponding amplitudes b_f^- and b_f^+ given by:

$$2R_1^{\pm} = R_{1f} + R_{1r} + k_{fr} + k_{rf} \pm \sqrt{(R_{1f} - R_{1r} + k_{fr} - k_{rf})^2 + 4k_{fr}k_{rf}} \tag{2.26}$$

$$b_f^{\pm} = \pm \frac{1}{R_1^+ - R_1^-} \left(\frac{M_{zf}(0)}{M_{0f}} - 1 \right) (R_{1f} - R_1^{\mp}) + \left(\frac{M_{zf}(0)}{M_{0f}} - \frac{M_{zr}(0)}{M_{0r}} \right) k_{fr} \tag{2.27}$$

An analytical solution to the SIR-FSE sequence can be derived by assuming that M_z=0 both for the free and the restricted pool after the last 180^0 pulse of the FSE sequence. This assumption has been verified using numerical simulations. The magnetization at the end of t_d is then given by:

$$\frac{M_{zf}(t_d^-)}{M_{0f}} = -\frac{R_{1f} - R_1^-}{R_1^+ - R_1^-} e^{-R_1^+ t_d} + \frac{R_{1f} - R_1^+}{R_1^+ - R_1^-} e^{-R_1^- t_d} + 1 \tag{2.28}$$

The effect of the inversion pulse is modelled by an instantaneous fraction (S_f) of magnetization after vs. before the pulse:

$$\frac{M_{zf}(t_d^+)}{M_{0f}} = S_f \frac{M_{zf}(t_d^-)}{M_{0f}} \tag{2.29}$$

Another period of free recovery of duration t_i follows before the FSE readout sequence is repeated. The magnetization of the restricted pool is similarly given by equations (2.25) - (2.29), by exchanging subscripts f and r. Combining equations (2.25)- (2.29) gives a signal equation that can be used to fit the measured signal to determine the seven parameters: R_{1f}, R_{1r}, F, k_r (with k_f given by $F \times k_r$), S_f, S_r, and M_{0f} (with M_{0r} given by $F \times M_{0f}$). As for the other methods presented here, R_{1r} is usually set equal to R_{1f}, while T_{2r} is assumed to be constant, by fixing a value for S_r, reducing the number of free parameters to five. The value of S_r can be determined by numerical simulations and depends on the lineshape of the restricted pool and T_{2r}. While S_f is expected to be -1, it needs to be fitted to take into account B_0 and B_1 field inhomogeneity." [20].

In summary, the off-resonance method (qMT-SPGR) requires shorter scan time and has been extensively tested in in vivo models, but the data analysis needs to be accompanied by static field (B_0), RF (B_1) and T_1 corrections. On the other hand, the on-resonance method (qMT-SIRFSE) does not require any separate dataset (e.g. B_0, B_1 or T_1 mapping), which facilitates its implementation and its reproducibility across sites. The results from a study by Dortch et al. [39] showed the feasibility of qMT-SIRFSE in human brain in vivo. However, multislice imaging is not possible with this approach due to MT effects on other slices caused by the refocusing pulse. Another drawback is the long duration of the scan, which can be challenging in clinical applications. Li et al. [40] optimized the protocol by maximizing precision efficiency and varying both inversion times (t_i) and delay time (t_d) instead of fixing t_d as the previous approach. It opened up the possibility of this method in the context of clinical MRI but even with this improvement, qMT-SPGR may be faster to image whole-brain at high-resolution. qMT-SIRFSE can be a better option in cases of high static/RF inhomogeneities, limited specific absorption rate (SAR) or high susceptibility differences especially in ultra-high field MRI [39].

CHAPTER 3 ON THE PRECISION OF MYELIN IMAGING: CHARACTERIZING EX VIVO SPINAL CORD WITH MRI AND HISTOLOGY

3.1 Methods

3.1.1 Tissue preparation

The myelin imaging methods were tested in ex vivo animal and human tissue. The dog spinal cord was imaged first because its dimensions are well-suited for exploration of microstructure on a typical preclinical scanner. In particular, the cord size allowed for good penetration of the fixative, and the imaging resolution required to avoid partial voluming did not push the limits of the MRI hardware. Once we were satisfied with the dog spinal cord results, we increased the imaging resolution to investigate the rat cord microstructure and to explore the portability of our protocol to other species. Finally, we imaged the ex vivo human spinal cord to show that human studies of cord microstructure are feasible ex vivo, and to set the stage for in vivo microstructural imaging of human spinal cord.

The tissue samples were prepared as follows:

- A sample of cervical dog spinal cord (post-fixed with paraformaldehyde 4%) was extracted and washed in Phosphate-buffered saline (PBS) solution for 5 days before scanning.
- A sample of rat spinal cord was perfused and post-fixed with paraformaldehyde 3% and glutaraldehyde 3% for 1 week, then immersed in PBS 1x for 5 days before scanning.
- A sample of thoracic human spinal cord (T6 vertebra) was post-fixed with paraformaldehyde 4% and glutaraldehyde 2% for 1 week, and then immersed in PBS 1x for 1 year before scanning.

Glutaraldehyde is expected to improve myelin fixation by killing cells quickly by crosslinking their proteins; It is commonly used in combination with formaldehyde to stabilize the specimens, but too high concentration of glutaraldehyde (more than 3%) can lead to large tissue shrinkage

[41-43]. Subsequently osmium tetroxide was applied to crosslink and stabilize the membrane lipids.

In general, fixation significantly reduces T_1 and T_2 relaxation times. This is because the crosslinking makes the tissue more rigid, and the dehydration necessary for embedding the tissue in resin removes the water content, which affects T_1 and T_2. The strongest reduction is observed in the T_1 relaxation time (up to 76%), "but the exact mechanisms responsible for these changes are still a matter of debate" [44].

3.1.2 MRI

All spinal cord samples were scanned on an Agilent 7T animal scanner equipped with 600 mT/m gradients. Each MRI acquisition was repeated twice. We moved out the dog and rat sample for scan-rescan experiment and we scanned the human sample without moving out it to investigate the upper bound of this experiment. The Gibbs ringing artifact is reduced by using the unring tool published at https://bitbucket.org/reisert/unring based on the algorithm described in [45].

3.1.2.1 Ex vivo dog spinal cord

For the dog spinal cord all myelin protocols were implemented using the same FOV of 9x9x2 mm^3 and a matrix size of 64x64.

1. **qMT-SIRFSE** (section 2.4.2) was implemented using a selective inversion recovery fast spin echo (FSE) sequence with 16 echoes, and echo spacing (ESP) of 6.4 ms. The selective inversion-recovery preparation was achieved using a 1ms hard pulse which effectively inverted the free water spins without affecting the macromolecular proton pool. The sequence used pre-delay time t_d=3.5s and was repeated with 30 different inversion time logarithmically spaced between 3.55ms and 10s, with 2 averages. The total acquisition time was 25 minutes. The fitting was performed using the qMTLab software [20] that implements the model of Gochberg and Gore [13].
2. **qMT-SPGR** (section 2.4.1): An RF-spoiled gradient echo sequence was used, TE/TR=2.46/25 ms, sinc MT pulses, α_{MT} =142^0 and 500^0, and nine off-resonance frequencies (Δ = 433, 800, 1000, 2000, 3000, 4000, 7000, 15000, and 17000 Hz). The protocol also included B_1 mapping using a fast spin echo sequence with two flip angles of

60^0 and 120^0 (TR=10s, ESP=8.97ms, 8 echoes), and B_0 mapping using a multiple gradient echo sequence (TR=300ms, ESP=2.79ms, $\alpha = 40^0$). The fitting was performed using the qMTLab software that implements the model of Sled and Pike [12].

3. **Proton Density Protocol** (section 2.2): Macromolecular Tissue Volume (MTV) was measured using the procedure described in section 2.2. A B_1 map was computed first using fast spin echo sequences with two excitation flip angles 60^0 and 120^0. Spoiled Gradient-Echo images (TE/TR=2.46/25ms, 100 dummy scans, 5 average) were acquired using flip angles of 4^0, 10^0 and 20^0. The fitting was performed using in-house fitting software.

4. **MET$_2$ imaging** (section 2.3): Multi-echo spin echo sequence was employed to acquire data with 32 echoes with the first echo time and echo spacing time (ESP) of 10ms, TR=3000ms with 8 averages. The fitting was performed using in-house fitting software.

All the MRI protocol settings for the ex vivo dog spinal cord are listed in Table 3.1

Table 3.1: MRI protocol for the ex vivo dog spinal cord

qMT-SIRFSE	qMT-SPGR	Proton Density Imaging	Multiexponential T_2
FOV= 9x9x2 mm^3, matrix size = 64x64, resolution 140x140x2000μm^3			
Selective inversion recovery fast spin echo sequence • 16 echoes, ESP= 6.4ms • 1ms hard pulse • pre-delay time t_d=3.5s • 2 averages • 30 TI logarithmically spaced between 3.55ms and 10s. • Total acquisition time = 15 minutes.	RF-spoiled gradient echo sequence • TE/TR=2.46/25 ms • $\alpha = 15^0$, 20 averages • sinc MT pulse • $\alpha_{MT} = 142^0 / 500^0$, • Δ = 400, 800, 1000, 2200, 3000, 4000, 7000, 16000, and 18000 Hz T1 map using IR spin echo sequence • TI=30,530,1030,1530 ms • TE/TR=10/1550ms B0 mapping using multiple gradient echo sequence • TR/ ESP=300ms/2.79ms • $\alpha = 40^0$ B1 mapping using fast spin echo sequence • $\alpha = 60^0/120^0$ • TR=10s • 8 echoes, ESP= 8.97ms Total acquisition time = 21 minutes.	RF-spoiled gradient echo sequence • $\alpha = 4^0/10^0/20^0$ • TE/TR=2.46/25ms • 5 averages B1 mapping using fast spin echo sequence • $\alpha = 60^0/120^0$ • TR=10s • 8 echoes, ESP= 8.97ms Total acquisition time = 4 minutes.	Multi-echo spin echo sequence • 32 echoes • ESP/TR=10ms/3s • 8 averages Total acquisition time = 25 minutes.

3.1.2.2 The ex vivo rat spinal cord

The MRI protocol settings for the ex vivo rat spinal cord are similar to the protocols for the ex vivo dog spinal cord and are listed in Table 3.2. The main differences are FOV, matrix size, the slice thickness and the number of averages.

Table 3.2: MRI protocol for the ex vivo rat spinal cord

qMT-SIRFSE	qMT-SPGR	Proton Density Imaging	Multiexponential T_2
FOV= 5x5x3 mm^3, matrix size = 32x32, zero-filling to 48x48;, resolution 156x156x3000μm^3			
Selective inversion recovery fast spin echo sequence • 16 echoes, ESP= 6.44ms • 1ms hard pulse • pre-delay time t_d=3.5s • 2 averages • 30 TI logarithmically spaced between 3.55ms and 10s. • Total acquisition time = 7.5 minutes.	**RF-spoiled gradient echo sequence** • TE/TR=2.12/25 ms • α=15^0, 64 averages • sinc MT pulse • α_{MT} =142^0 / 500^0, • Δ = 433, 800, 1000, 2200, 3000, 4000, 7000, 16000, and 18000 Hz **T1 map using IR spin echo sequence** • TI=30,530,1030,1530 ms • TE/TR=10/1550ms **B0 mapping using multiple gradient echo sequence** • TR/ ESP=300ms/1.82ms • α =40^0 **B1 mapping using fast spin echo sequence** • α = 60^0/120^0 • TR=10s • 8 echoes, ESP= 6.44ms Total acquisition time = 21 minutes.	**RF-spoiled gradient echo sequence** • α=4^0/10^0/20^0/30^0 • TE/TR=2.12/25ms • 64 averages **B1 mapping using fast spin echo sequence** • α = 60^o/120^o • TR=10s • 8 echoes, ESP= 6.44ms Total acquisition time = 5 minutes.	**Multi-echo spin echo sequence** • 32 echoes • ESP/TR=10ms/3s • 9 averages Total acquisition time = 14.5 minutes.

3.1.2.3 The ex vivo human spinal cord

The MRI protocol settings for the ex vivo human spinal cord are similar to the protocols for the ex vivo dog spinal cord and are listed in Table 3.3. The main differences are FOV, matrix size, the slice thickness and the number of averages.

Table 3.3: MRI protocol for the ex vivo human spinal cord

qMT-SIRFSE	qMT-SPGR	Proton Density Imaging	Multiexponential T_2
FOV= 10x10x3 mm^3, matrix size = 64x64, resolution 140x140x2000μm^3			
Selective inversion recovery fast spin echo sequence • 16 echoes, ESP= 6.18ms • 1ms hard pulse • pre-delay time t_d=3.5s • 2 averages • 30 TI logarithmically spaced between 3.55ms and 10s. • Total acquisition time = 15 minutes.	**RF-spoiled gradient echo sequence** • TE/TR=2.38/25 ms • α=15^0, 64 averages • sinc MT pulse • α_{MT}=142^0 / 500^0, • Δ = 433, 800, 1000, 2200, 3000, 4000, 7000, 16000, and 18000 Hz **T1 map using IR spin echo sequence** • TI=30,530,1030,1530 ms • TE/TR=10/1550ms **B0 mapping using multiple gradient echo sequence** • TR/ ESP=300ms/1.78ms • α =40^0 **B1 mapping using fast spin echo sequence** • α = 60^0/120^0 • TR=10s • 8 echoes, ESP= 6.18ms Total acquisition time = 42 minutes.	**RF-spoiled gradient echo sequence** • α=4^0/10^0/20^0/30^0 • TE/TR=2.38/25ms • 64 averages **B1 mapping using fast spin echo sequence** • α = 60^0/120^0 • TR=10s • 8 echoes, ESP= 6.18ms Total acquisition time = 10 minutes.	**Multi-echo spin echo sequence** • 32 echoes • ESP/TR=10ms/3s • 8 averages Total acquisition time = 29 minutes.

3.1.3 Histology

Following the MRI acquisition, the spinal cord specimens were osmified (2% OsO_4 for 2 hours), embedded in EMbed 812 Resin, cut using a microtome and polished. A scanning electron microscope (Low-angle backscattered electron mode) (JEOL 7600F) was used to image an entire slice of the spinal cord at a resolution of 0.26µm/pixel [41-43] .

For the dog SC sample, myelin volume fraction (MVF) was segmented using an adaptive OTSU algorithm [46]. The poor compaction of the myelin sheaths made the segmentation challenging and led to slight overestimation of the MVF. For the rat SC and human SC sample the myelin compaction was improved (thanks to the use of glutaraldehyde), so the MVF was estimated using the automatic segmentation open software AxonSeg [47]. In all cases, MVFs were then registered to the MRI-based metrics using an affine transformation.

3.1.4 Statistics

A voxel-wise correlation matrix (Pearson's correlation coefficient) was generated in order to assess the scan-rescan repeatability of each MRI-based myelin metric, as well as the correlation between metrics in the white matter and in the whole spinal cord. Pearson's correlation coefficient was chosen because (i) the linearity has long been assumed in the literature when considering the relationship between the myelin metrics [15, 17, 18, 48, 49]; (ii) the scatter plots shown in Figure 3.3-Figure 3.6, Figure 3.9-Figure 3.12, Figure 3.15-Figure 3.18 predict a linear trend between those metrics. We set a p-value threshold of .0001 to determine if a correlation is statistically significant.

3.2 Results

3.2.1 Ex vivo dog spinal cord

Figure 3.1 shows the scan-rescan of the MRI-based metrics, as well as the histological image of the same tissue sample. These metrics are sensitive to myelin as suggested by: (i) significantly lower values in the gray matter than in the WM, (ii) values close to zero in the water surrounding the sample, (iii) small coefficient of variation in the WM, corroborated by the small variation of myelin content between the different tracts of the spinal cord [50]. It can be seen that all the MRI-based metrics predict a similar trend in the myelin content distribution, with higher values in the dorsal column that are consistent with histology.

Figure 3.2 presents the Pearson's correlation coefficients using voxel-wise analysis between the MRI-based metrics and MVF from histology in white matter and whole spinal cord. Scan-rescan metrics (diagonal values) were correlated highly in WSC (0.87-0.96) and moderately in WM (0.65-0.78). High correlation in WSC (0.83-0.95) and moderate correlation (0.47-0.7) in WM were also observed between all the MRI-based metrics. Correlations with histology were lower (0.66-0.75 in WSC and 0.24-0.29 in WM), but statistically significant ($p<.0001$).

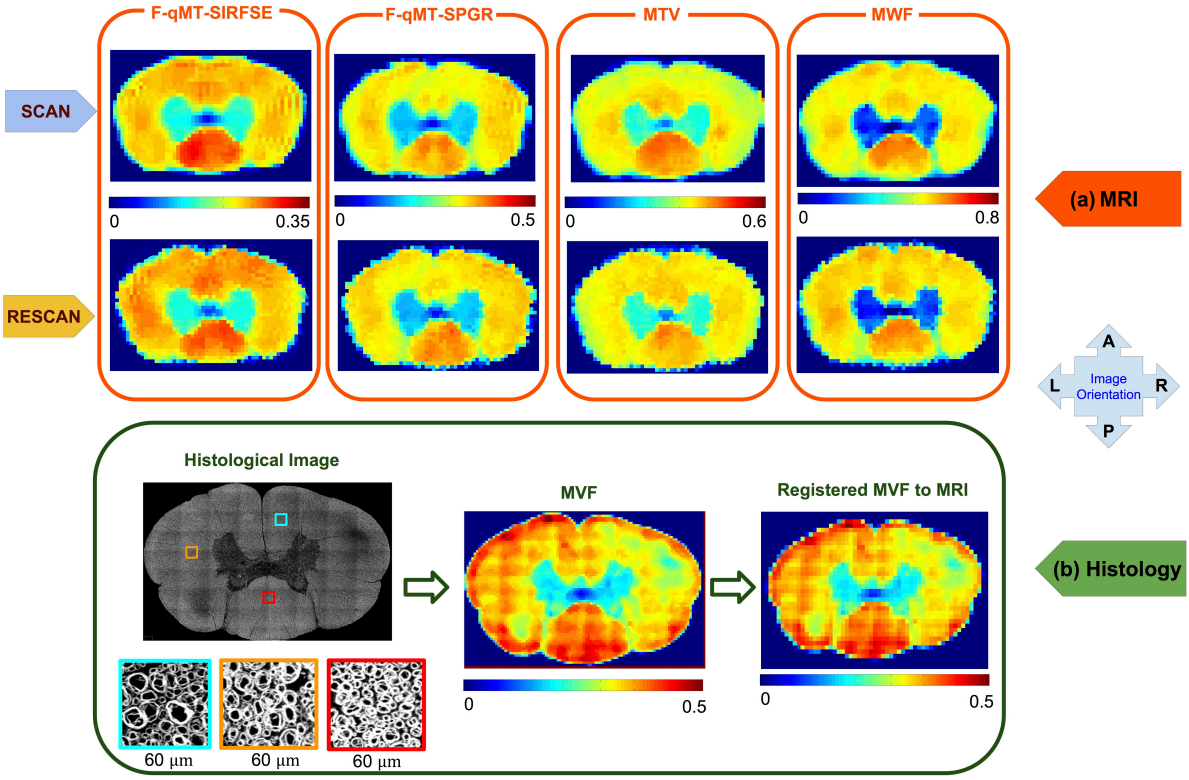

Figure 3.1: Dog spinal cord: (a) Scan-Rescan results of four MRI-based myelin metrics: F using qMT-SIRFSE, F using qMT-SPGR, MTV and MWF; (b) Histology from scanning Electron Microscopy and zoomed-in views of three regions.

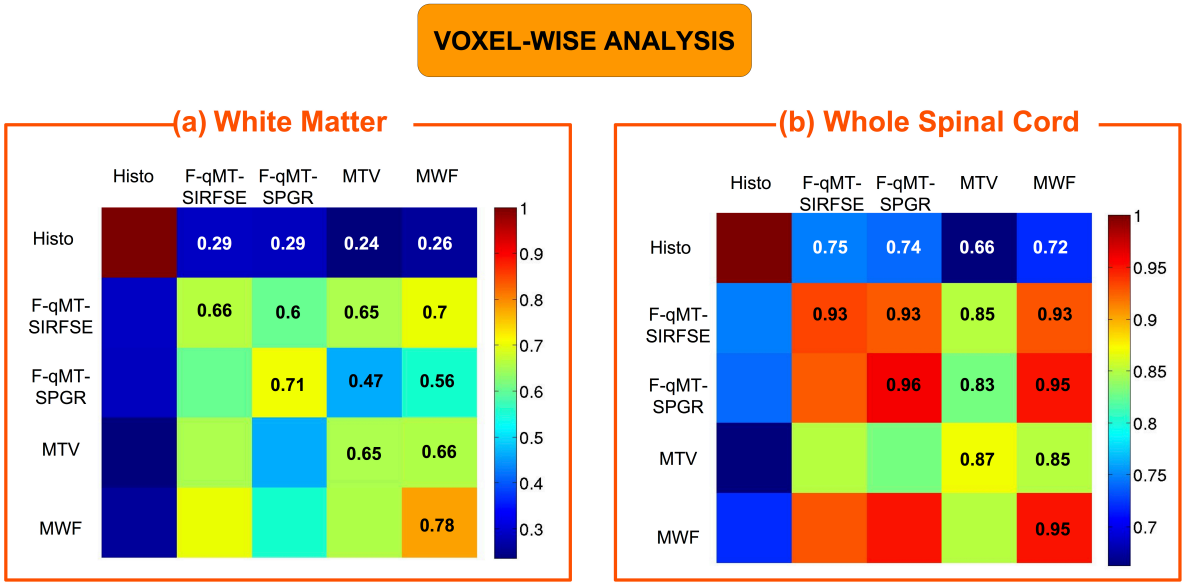

Figure 3.2: Dog spinal cord: Correlation Matrices between MRI-based metrics and MVF from histology using voxel-wise analysis in (a) white matter (WM) and (b) whole spinal cord (WSC).

Along the diagonal are the test-retest correlation coefficients for each metric, except for the histology that was only performed once.

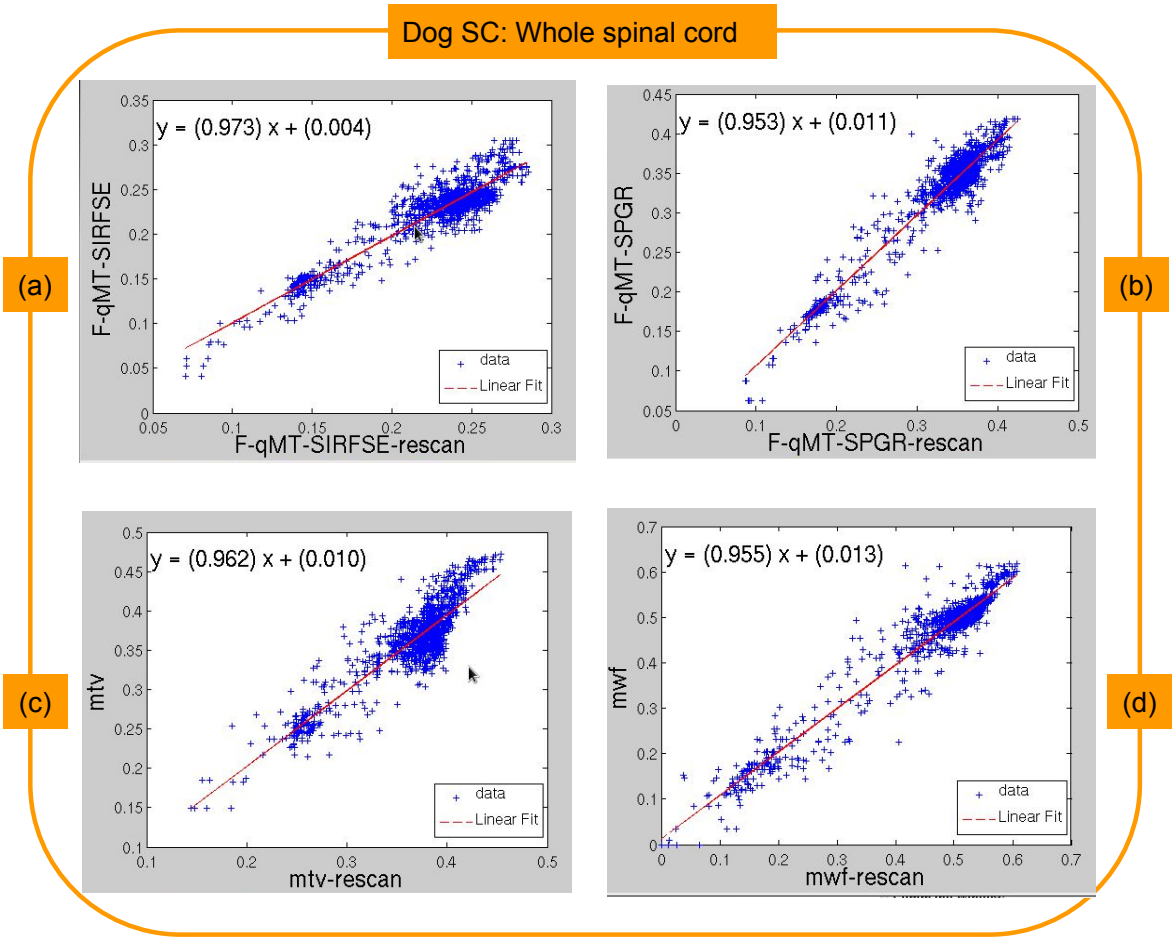

Figure 3.3: Dog spinal cord: Scatter plots in whole spinal cord comparing the metrics obtained from scan and rescan of (a) F-qMT-SIRFSE; (b) F-qMT-SPGR; (c) MTV; (d) MWF.

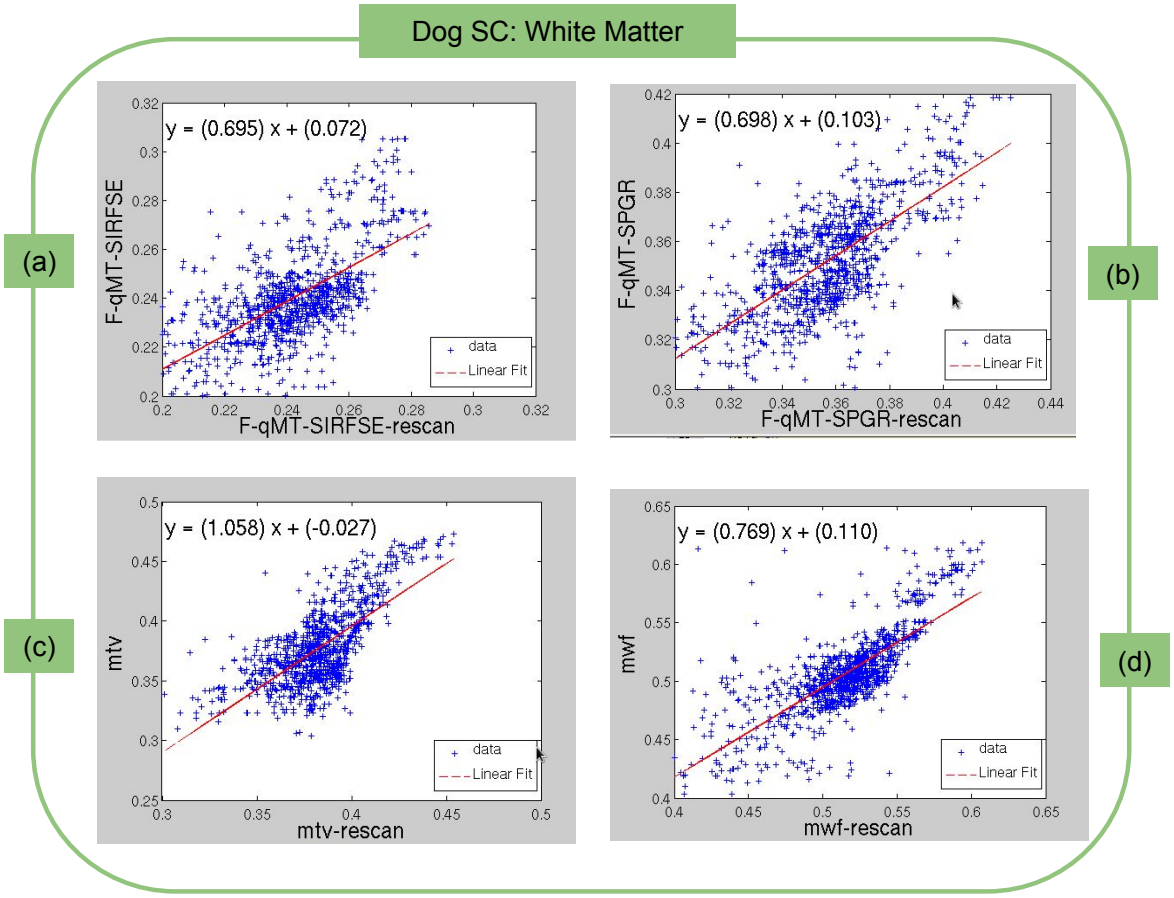

Figure 3.4: Dog spinal cord: Scatter plots in white matter comparing the metrics obtained from scan and rescan of (a) F-qMT-SIRFSE; (b) F-qMT-SPGR; (c) MTV; (d) MWF.

The scatter plots obtained from comparing the scan and rescan metrics are shown in Figure 3.3 (whole spinal cord) and in Figure 3.4 (white matter only). Pairwise comparisons presented in Figure 3.5 (whole spinal cord) and Figure 3.6, (white matter only). The scatter plots predict a linear trend in the relationship between the MRI-based metrics, which justifies the use of Pearson's correlation coefficient for statistics. Qualitatively, the linearity is more pronounced when considering the whole spinal cord in the scatter plots due to the good contrast between gray matter and white matter.

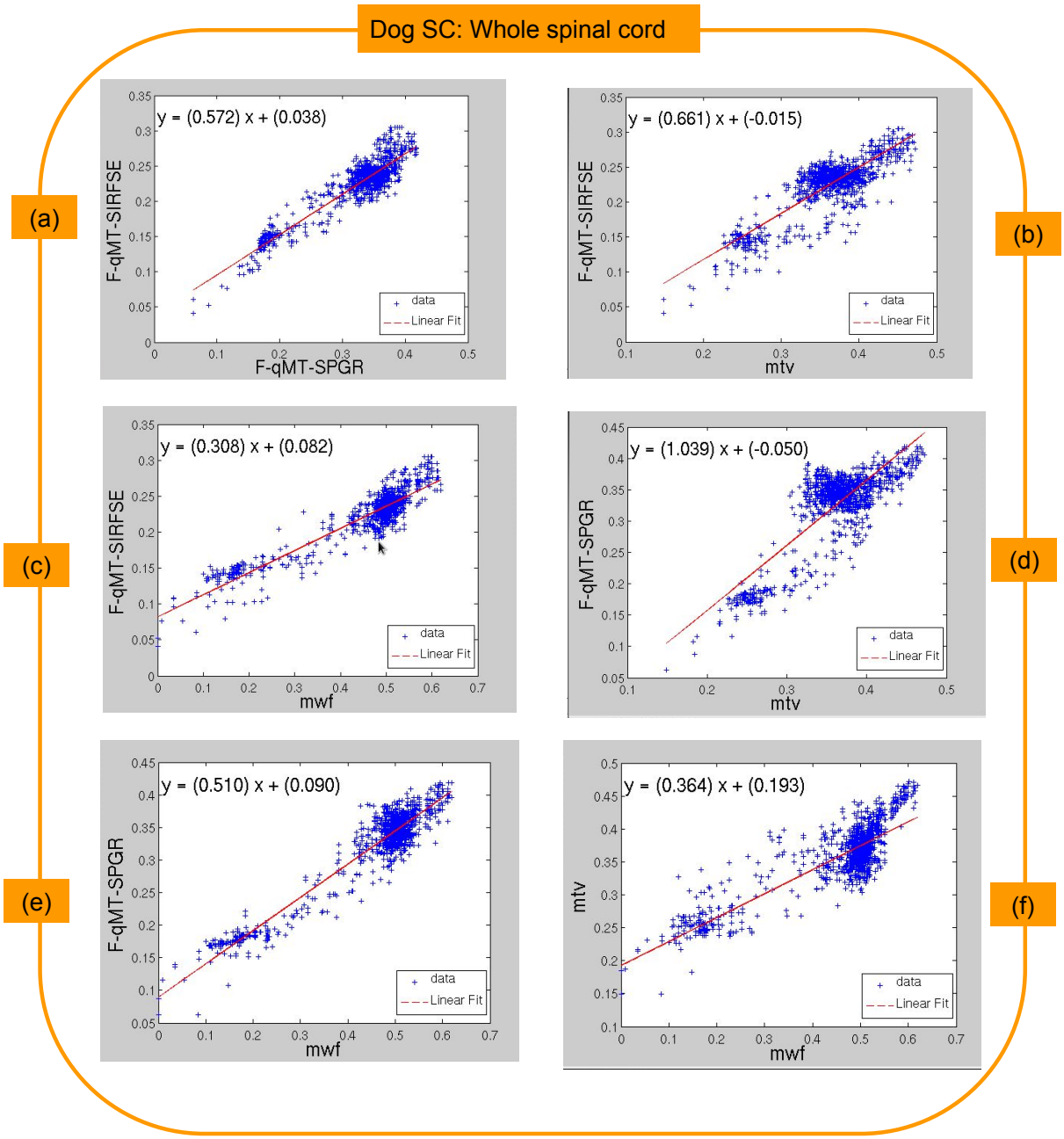

Figure 3.5: Dog spinal cord: Pairwise comparisons of MRI metrics in whole spinal cord using scatter plots of (a) F-qMT-SIRFSE and F-qMT-SPGR; (b) F-qMT-SIRFSE and MTV; (c) F-qMT-SIRFSE and MWF; (d) F-qMT-SPGR and MTV; (e) F-qMT-SPGR and MWF; (f) MTV and MWF.

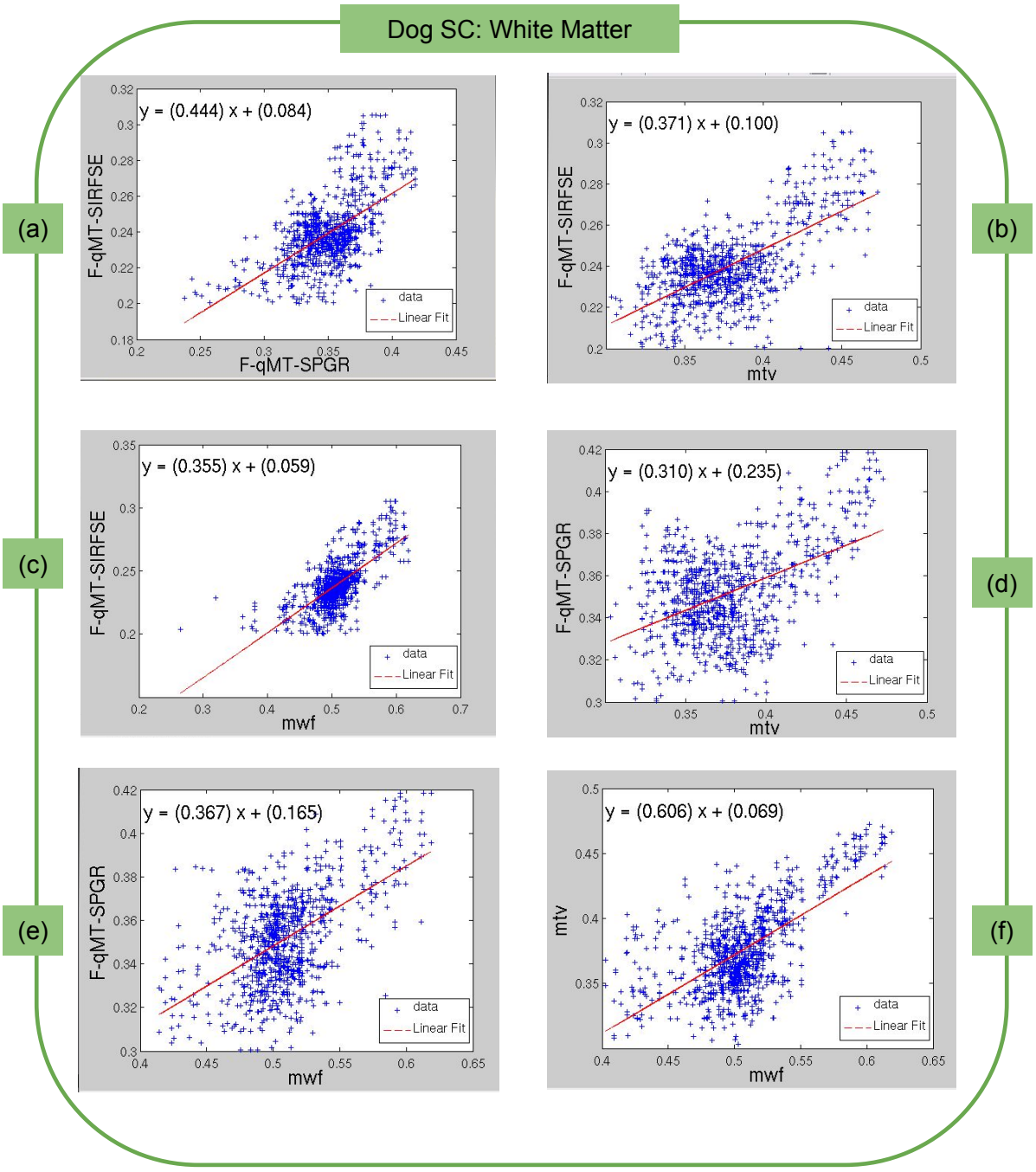

Figure 3.6: Dog spinal cord: Pairwise comparisons of MRI metrics in the dog WM using scatter plots of (a) F-qMT-SIRFSE and F-qMT-SPGR; (b) F-qMT-SIRFSE and MTV; (c) F-qMT-SIRFSE and MWF; (d) F-qMT-SPGR and MTV; (e) F-qMT-SPGR and MWF; (f) MTV and MWF.

3.2.2 Ex vivo rat spinal cord

Figure 3.7 shows the scan-rescan of the MRI-based metrics, as well as the histological image of the same tissue sample of the ex vivo rat spinal cord. Qualitatively, the observations were similar with what was observed in the ex vivo dog spinal cord results. However, the myelin metric from qMT-SIRFSE showed lower contrast between WM and GM compared to the other methods and histological images.

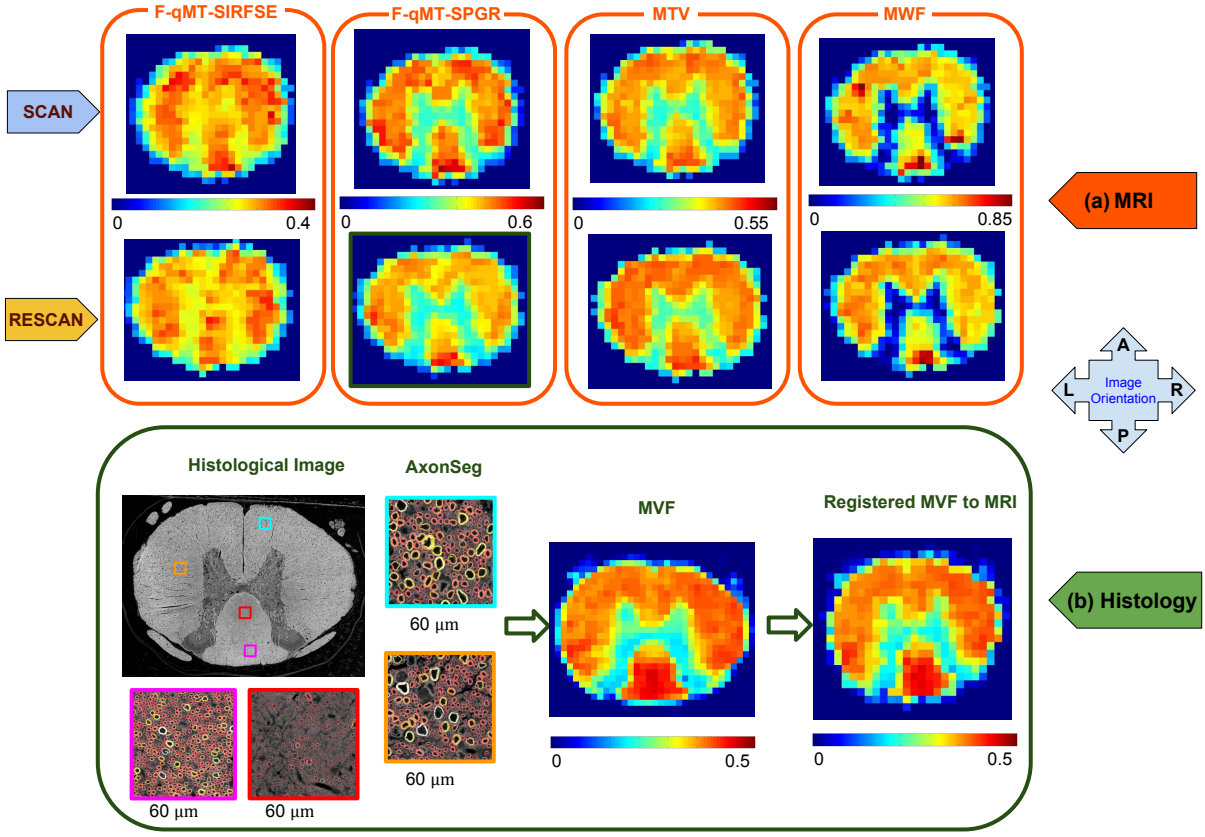

Figure 3.7: Rat spinal cord: (a) Scan-Rescan comparison of four MRI-based myelin metrics: F using qMT-SIRFSE, F using qMT-SPGR, MTV and MWF; (b) Histology from scanning electron microscopy and zoomed-in views of four regions after segmenting myelin using the open-source software AxonSeg [47].

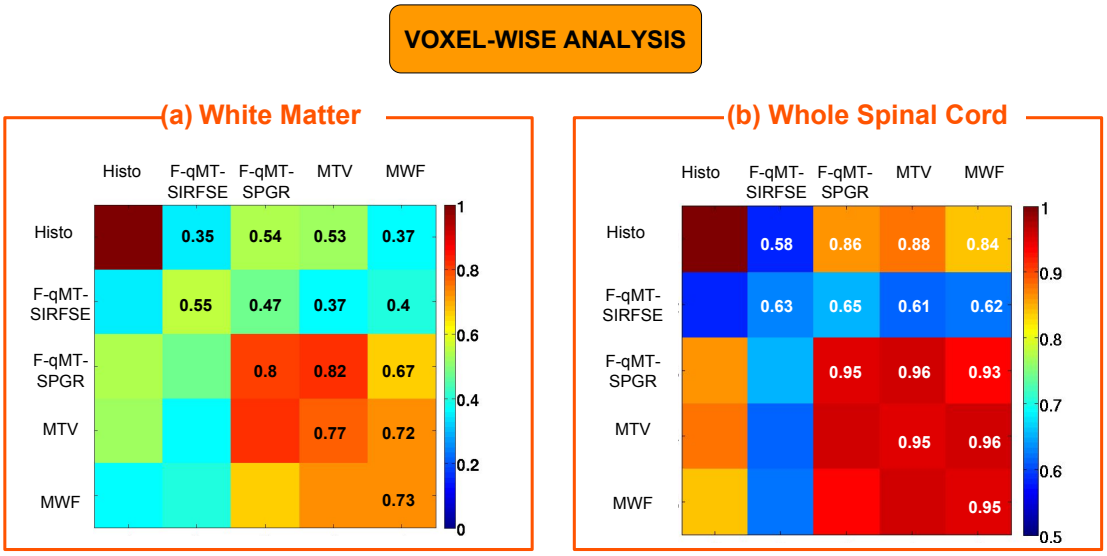

Figure 3.8: Rat spinal cord: Correlation matrices between MRI-based metrics and MVF from histology using voxel-wise analysis in (a) white matter (WM) and (b) whole spinal cord (WSC). Along the diagonal are the test-retest correlation coefficients for each metric, except for the histology which was only performed once.

Figure 3.8 presents the Pearson's correlation coefficients using voxel-wise analysis between the MRI-based metrics and MVF from histology in white matter and whole spinal cord. Three of the techniques (F-qMT-SPGR, MTV, MWF) were correlated highly in WSC (0.95) and moderately in WM (0.73-0.8), as can be seen from the diagonal entries in the correlation matrices. High correlation in WSC (0.93-0.96) and moderate correlation (0.67-0.82) in WM were also observed between these MRI-based metrics.

The scan-rescan result for F from qMT-SIRFSE showed lower correlations (0.63 in WSC and 0.55 in WM) and this metric was correlated moderately with the other MRI-based metrics in WSC (0.61-0.65) and in WM (0.35-0.47).

Correlations with histology were lower (0.58-0.88 in WSC and 0.35-0.54 in WM), but statistically significant ($p<.0001$).

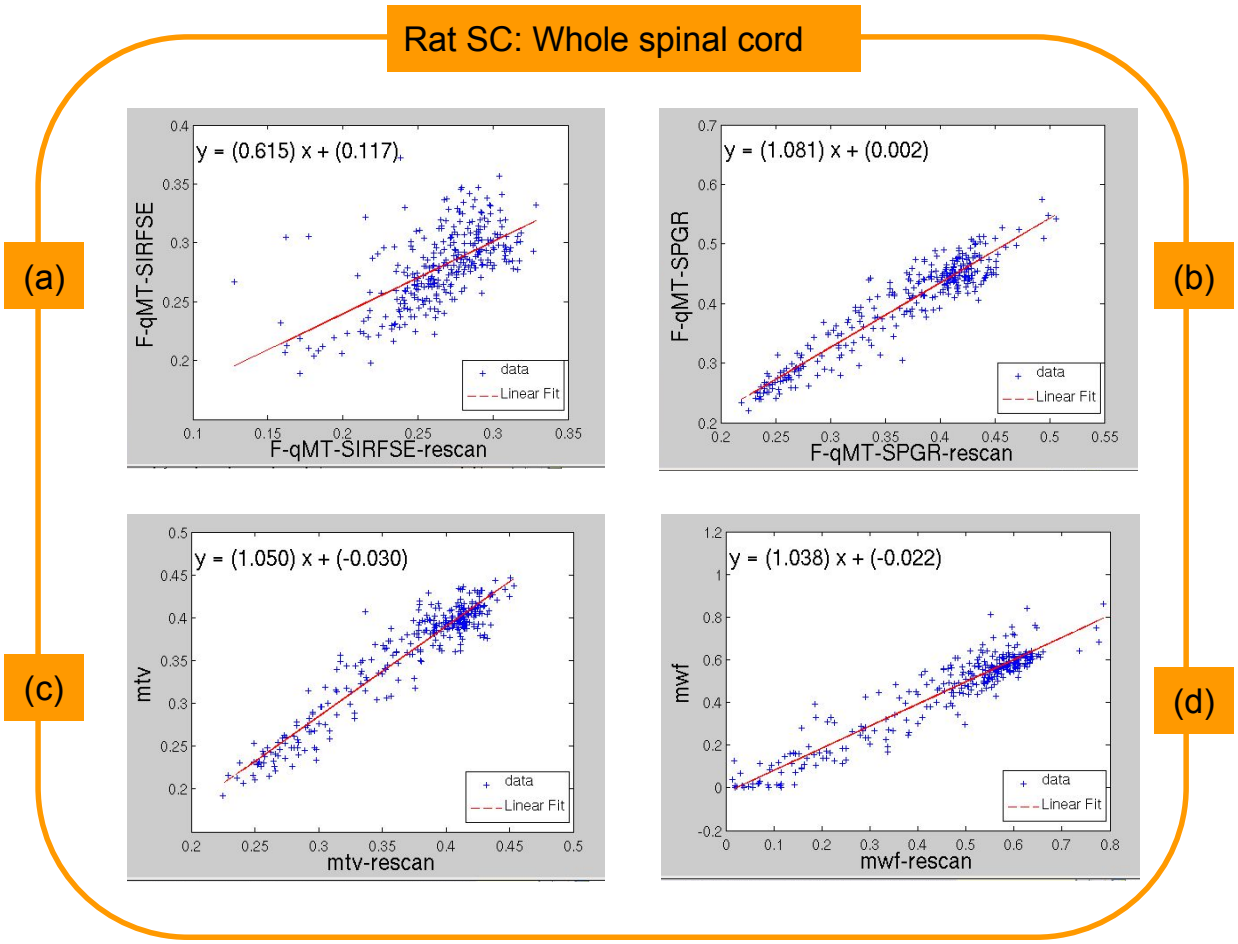

Figure 3.9: Rat spinal cord: Scatter plots in whole spinal cord comparing the metrics obtained from scan and rescan of (a) F-qMT-SIRFSE; (b) F-qMT-SPGR; (c) MTV; (d) MWF.

Scatter plots between scan and rescan metrics are shown in Figure 3.9 when taking the whole spinal cord into account and in Figure 3.10 when considering white matter only. Scatter plots in whole spinal cord and in white matter only between MRI-based metrics are presented in Figure 3.11 and Figure 3.12, respectively. Similar to the observations in the dog spinal cord data, those scatter plots predict a linear trend in the relationship between the MRI-based metrics and the linearity looks more pronounced when considering the whole spinal cord compared to the case of white matter only.

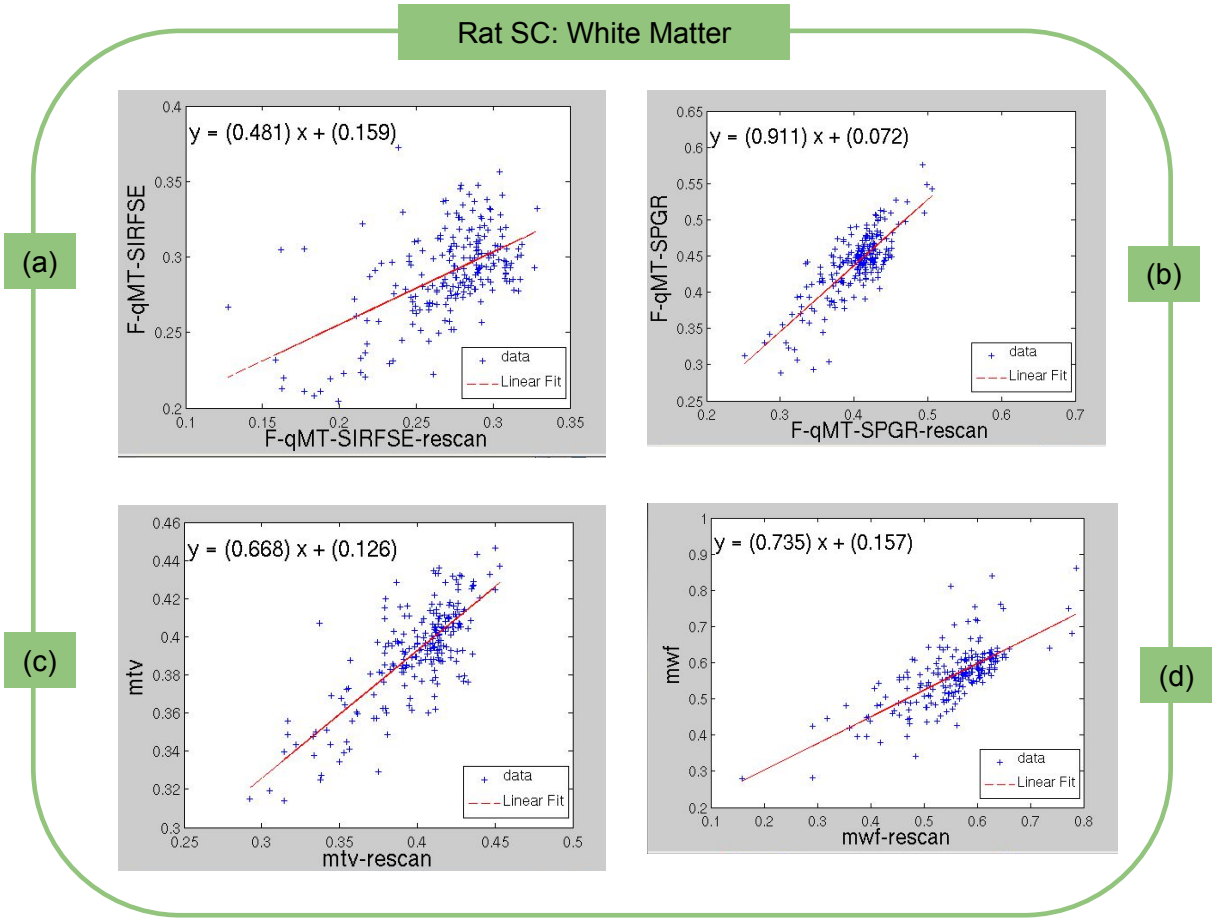

Figure 3.10: Rat spinal cord: Scatter plots in white matter comparing the metrics obtained from scan and rescan of (a) F-qMT-SIRFSE; (b) F-qMT-SPGR; (c) MTV; (d) MWF.

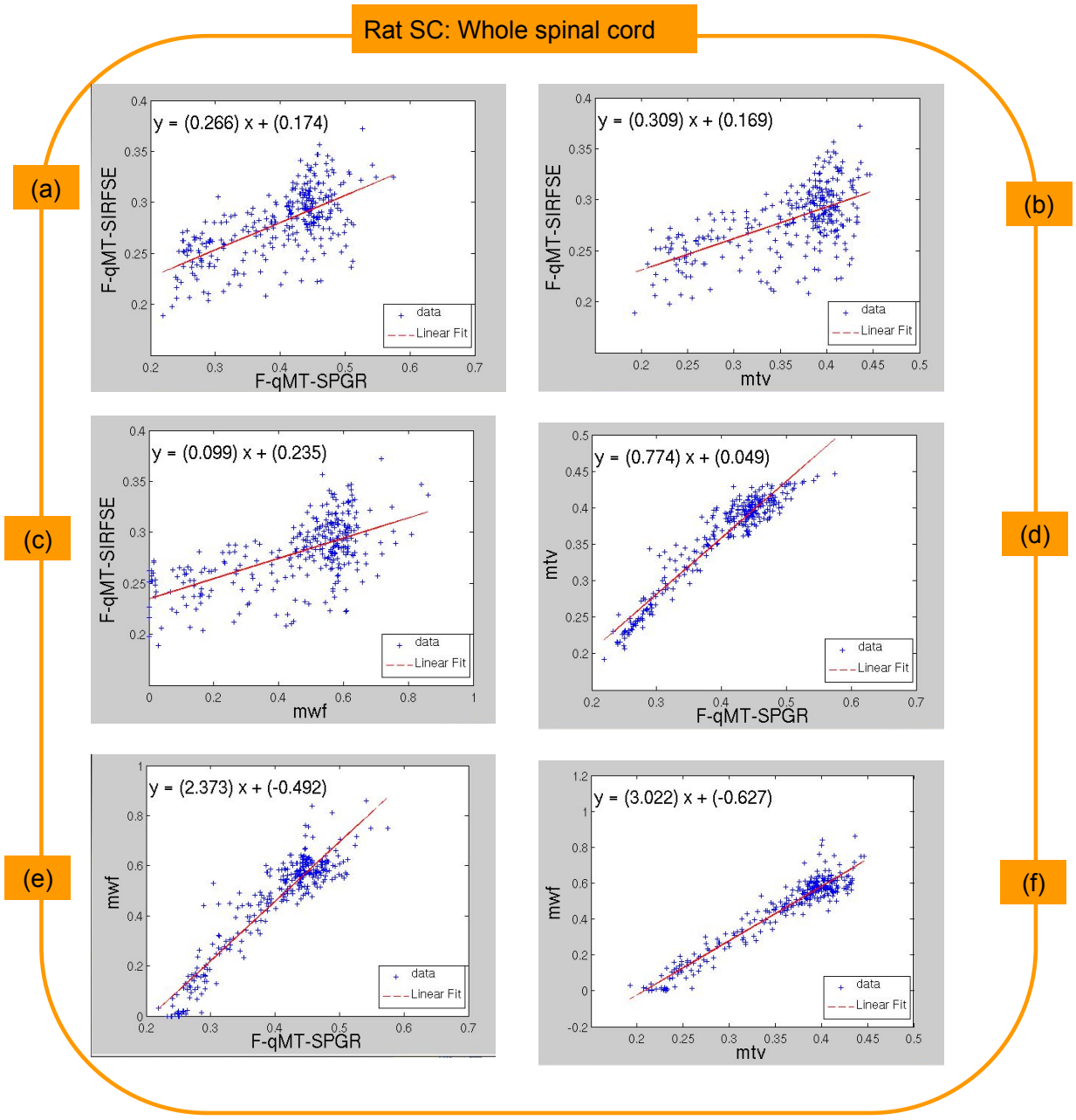

Figure 3.11: Rat spinal cord: Pairwise comparison of MRI metrics using scatter of plots of (a) F-qMT-SIRFSE and F-qMT-SPGR; (b) F-qMT-SIRFSE and MTV; (c) F-qMT-SIRFSE and MWF; (d) F-qMT-SPGR and MTV; (e) F-qMT-SPGR and MWF; (f) MTV and MWF.

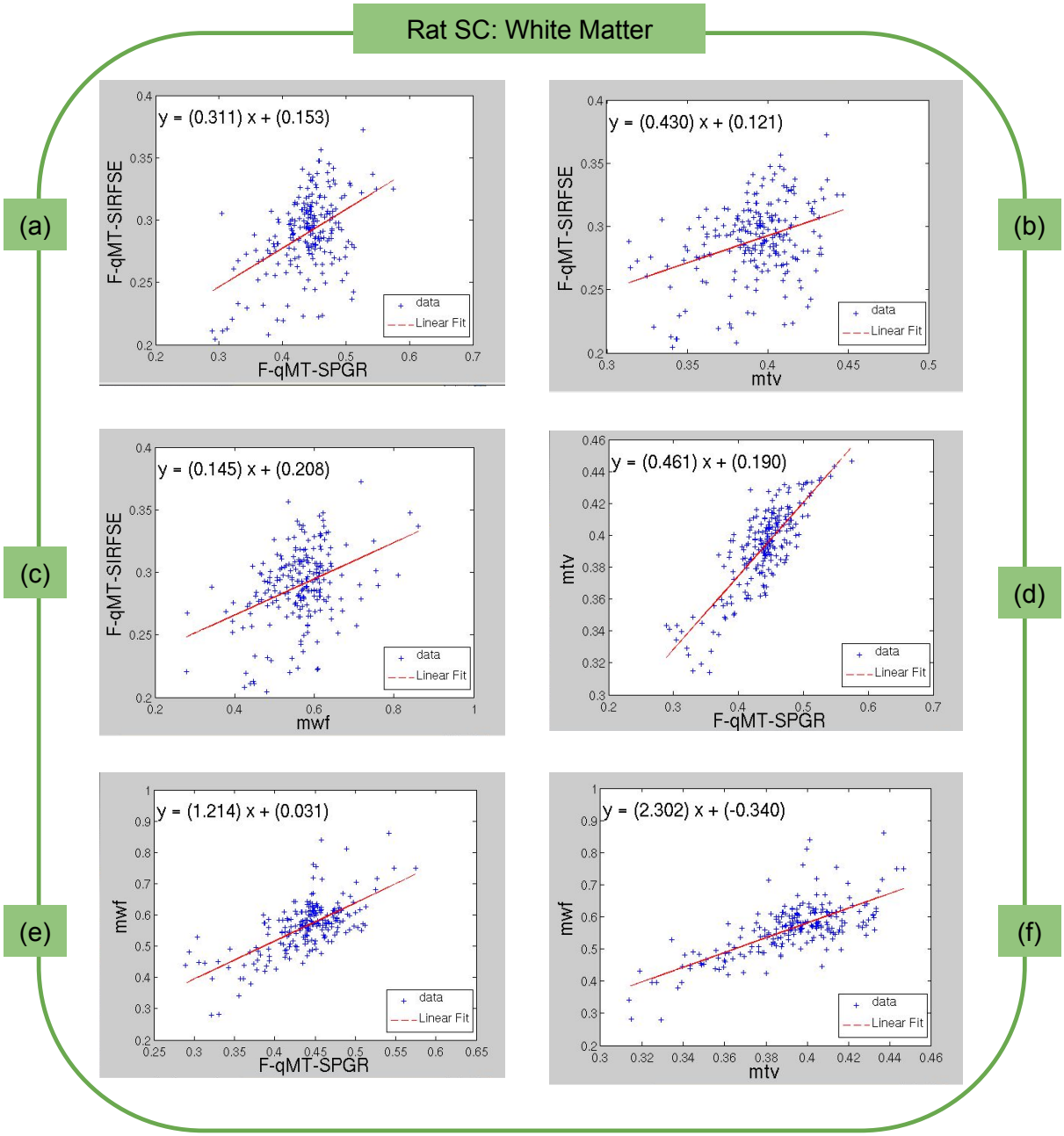

Figure 3.12: Rat spinal cord: Pairwise comparison of MRI metrics using scatter of plots of (a) F-qMT-SIRFSE and F-qMT-SPGR; (b) F-qMT-SIRFSE and MTV; (c) F-qMT-SIRFSE and MWF; (d) F-qMT-SPGR and MTV; (e) F-qMT-SPGR and MWF; (f) MTV and MWF.

3.2.3 Ex vivo human spinal cord

Figure 3.13 shows the scan-rescan of the MRI-based metrics, as well as the histological image of the same tissue sample of the ex vivo human spinal cord. Qualitatively, the observations were similar with the ex vivo dog spinal cord results.

Figure 3.13: Human spinal cord: (a) Scan-Rescan results of four MRI-based myelin metrics: F using qMT-SIRFSE, F using qMT-SPGR, MTV and MWF; (b) Histology from scanning Electron Microscopy and zoomed-in views of four regions after segmenting myelin using the open-source software AxonSeg [47].

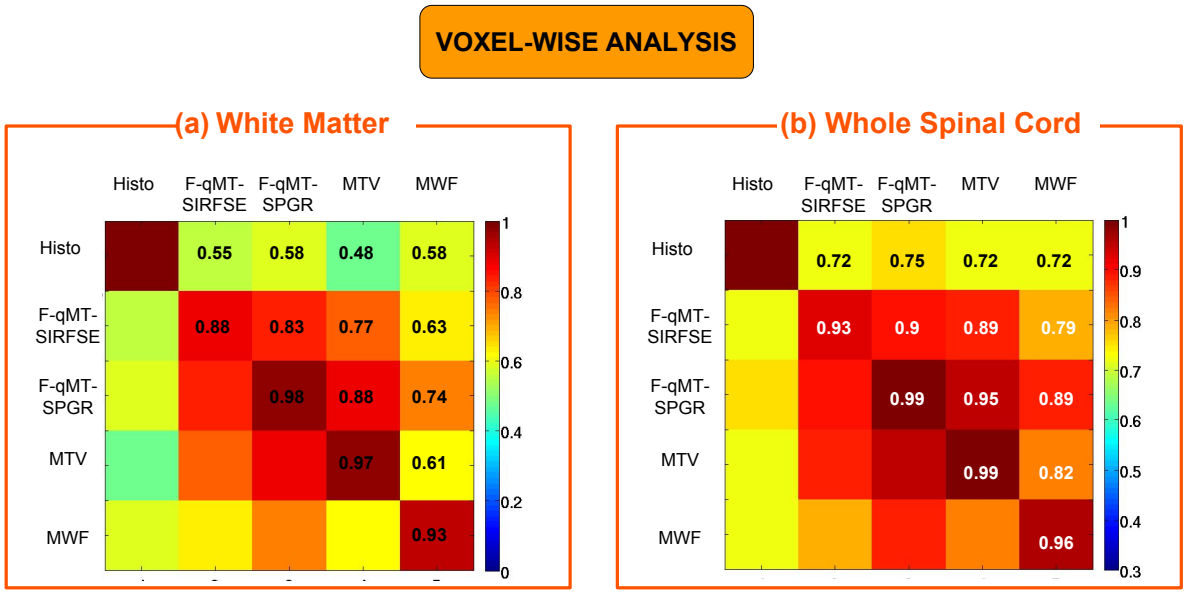

Figure 3.14: Human spinal cord: Correlation matrices for MRI-based metrics using voxel-wise analysis in (a) white matter (WM) and (b) whole spinal cord (WSC). Along the diagonal are the test-retest correlation coefficients for each metric.

Figure 3.14 presents the Pearson's correlation coefficients using voxel-wise analysis between the MRI-based metrics in white matter and whole spinal cord. Scan-rescan metrics (diagonal values) were correlated highly in WSC (0.93-0.99) and in WM (0.88-0.98). High correlation in WSC (0.79-0.95) and moderate to high correlation (0.61-0.88) in WM were also observed between all the MRI-based metrics. Correlations with histology were lower (0.72-0.75 in WSC and 0.48-0.58 in WM), but statistically significant ($p<.0001$).

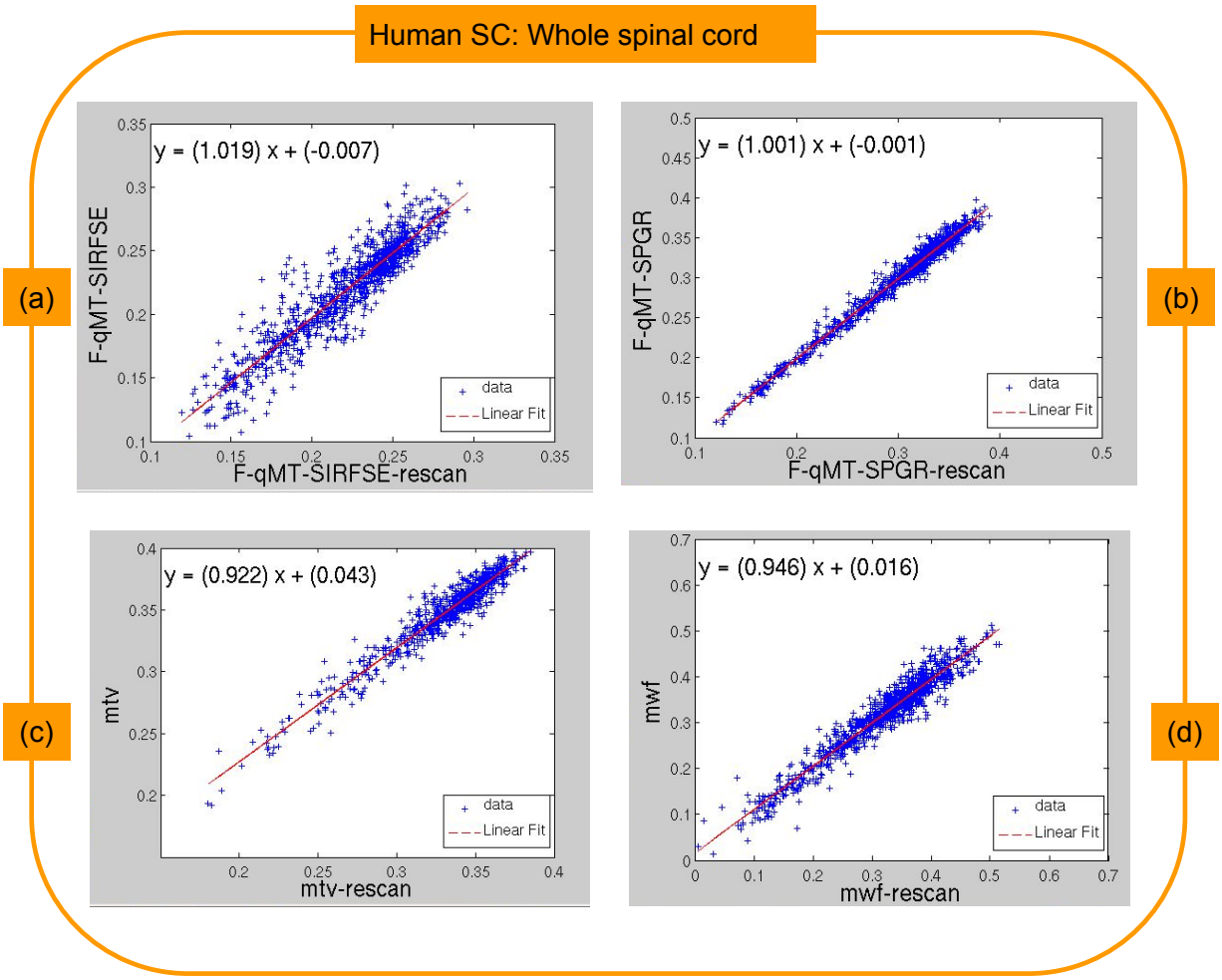

Figure 3.15: Human spinal cord: Scatter plots in whole spinal cord comparing the metrics obtained from scan and rescan of (a) F-qMT-SIRFSE; (b) F-qMT-SPGR; (c) MTV; (d) MWF.

Scatter plots between scan and rescan metrics are shown in Figure 3.15 when taking the whole spinal cord into account and in Figure 3.16 when considering white matter only. Scatter plots in whole spinal cord and in white matter only between MRI-based metrics are presented in Figure 3.17 and Figure 3.18, respectively. Similar to the observations in the dog spinal cord data, a linear trend in the relationship between the MRI-based metrics is predicted in those scatter plots and the linearity looks more pronounced when considering the whole spinal cord compared to the case of white matter only.

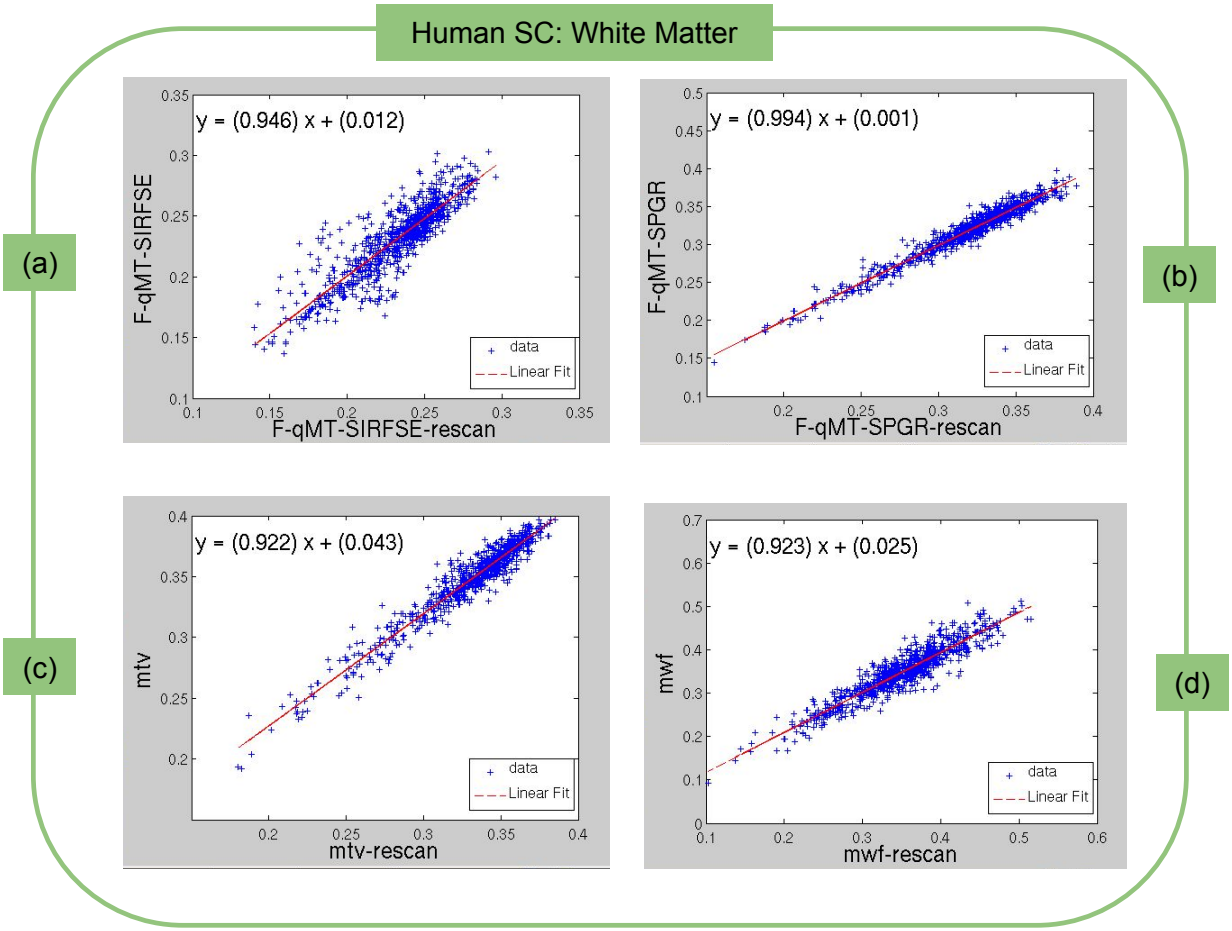

Figure 3.16: Human spinal cord: Scatter plots in white matter comparing the metrics obtained from scan and rescan of (a) F-qMT-SIRFSE; (b) F-qMT-SPGR; (c) MTV; (d) MWF.

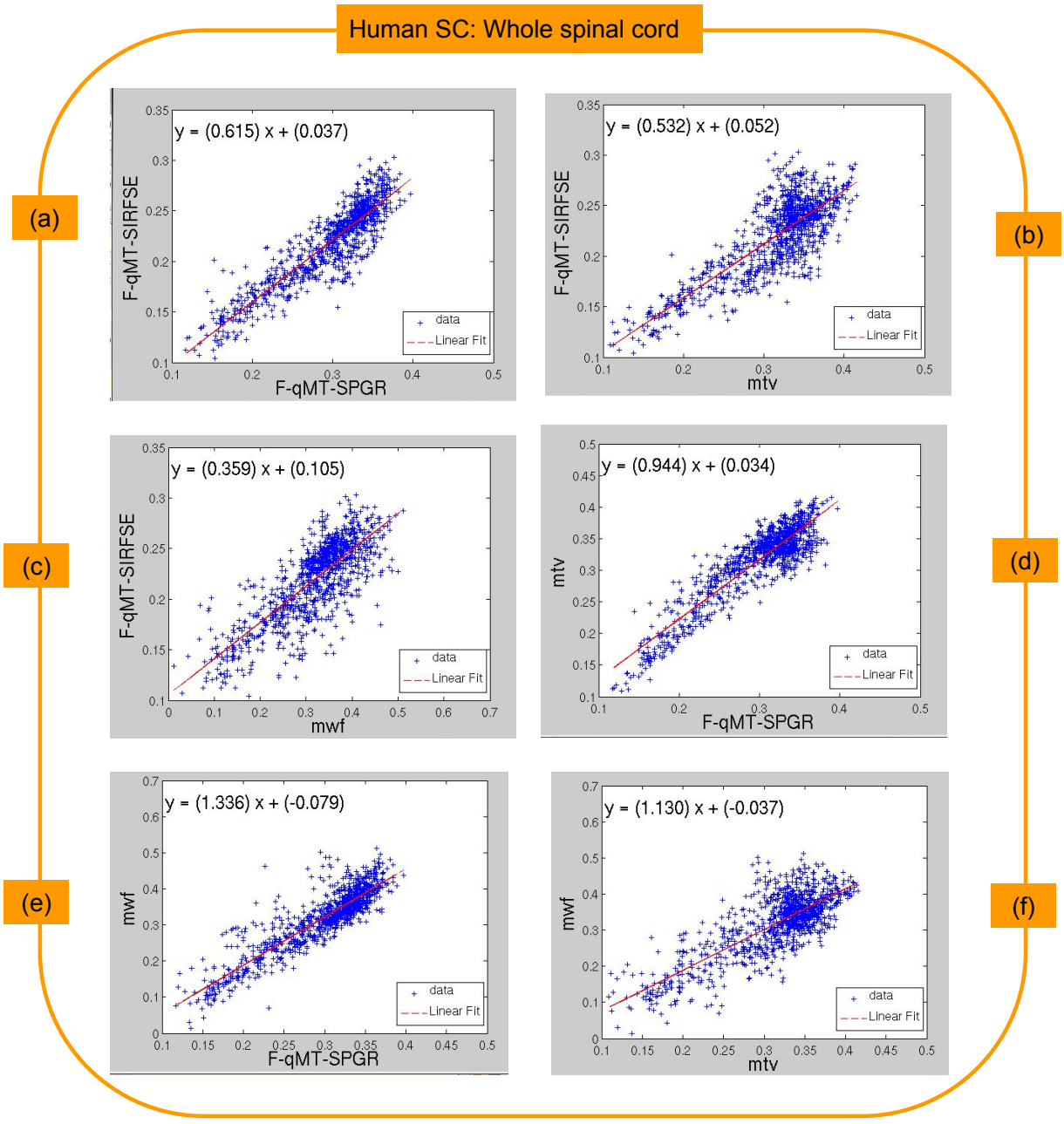

Figure 3.17: Human spinal cord: Pairwise comparison of MRI metrics using scatter of plots of (a) F-qMT-SIRFSE and F-qMT-SPGR; (b) F-qMT-SIRFSE and MTV; (c) F-qMT-SIRFSE and MWF; (d) F-qMT-SPGR and MTV; (e) F-qMT-SPGR and MWF; (f) MTV and MWF.

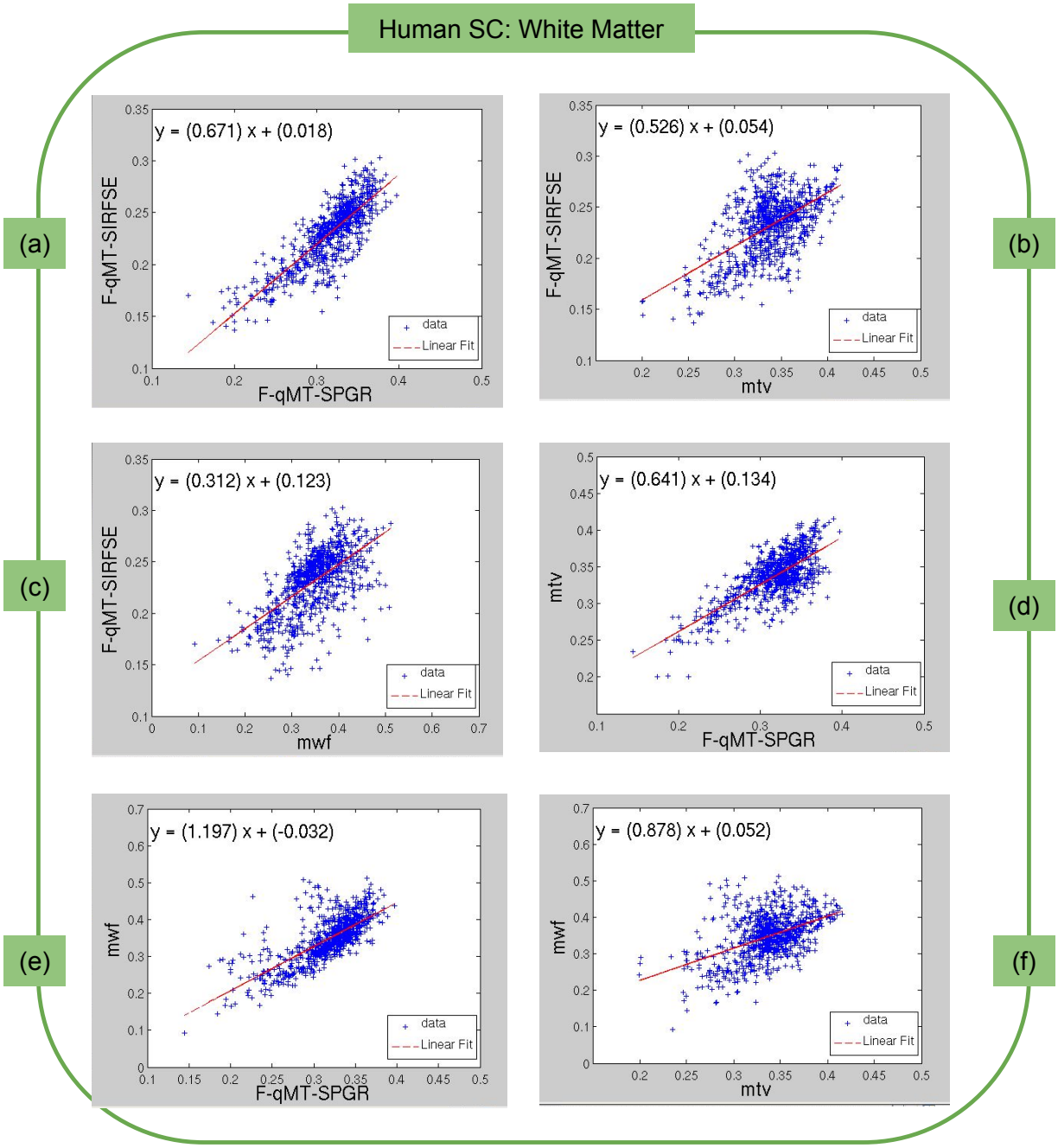

Figure 3.18: Human spinal cord: Pairwise comparison of MRI metrics using scatter of plots of (a) F-qMT-SIRFSE and F-qMT-SPGR; (b) F-qMT-SIRFSE and MTV; (c) F-qMT-SIRFSE and MWF; (d) F-qMT-SPGR and MTV; (e) F-qMT-SPGR and MWF; (f) MTV and MWF.

3.3 Discussion

3.3.1 Method implementation

The spinal cord is an interesting and important model tissue for biomedical research. However, MRI of the spinal cord is challenging and increases the level of complexity due to its rather small structure in contrast to that of the brain. Therefore, making a technique robust is more difficult in spinal cord model especially in quantitative MRI. Moreover, successful implementation of qMRI methods in different sites requires a lot of efforts and careful attentions. Miscalibrating any of dozens parameters during acquisitions as well as data processing may lead to anywhere from minor to major impact on the accuracy of the results.

One of the common miscalibrations is deriving a wrong B_1 map. Figure 3.19 (a) shows the T_1 map from proton density imaging (using variable flip angle SPGR images), with insufficient spoiling SPGR images and incorrect B_1 map. This B_1 map was derived from the dual-angle fast spin echo images with insufficiently long TR. The dual-angle method discussed in section 2.3 assumes the longitudinal magnetization fully recovered to the equilibrium magnetization after each TR. This is not necessarily true if TR is not sufficiently long.

Another common miscalibration is insufficient spoiling in methods using SPGR sequences. These methods assume no residual transverse magnetization at the end of the TR. This assumption is not realistic since short TR is required for steady state sequences. Gradient spoiling is usually combined with RF spoiling with quadratic phase increment, which is standard to get rid of the residual transverse magnetization [25]. In addition, the choice of excitation pulses may also influences the degree of spoiling. Moreover, the whole sequence is repeated until steady-state is achieved and data are only acquired when SS is reached, which might take about 200 repetitions [20]. Therefore, a reasonable number of dummy scans should be taken into consideration. Figure 3.19 (b) emphasizes the impact of insufficient spoiling SPGR images on the fitted values of T_1, where T_1 values in water (surrounding the spinal cord) were underestimated (around 1s). Given a linear relationship between 1/(1-MTV) and $1/T_1$ [15], underestimated T_1 also means that MTV will be overestimated. Figure 3.19 (c) depicts the asymmetry of F from qMT-SPGR derived from insufficiently spoiled SPGR images and an imperfect B_1 map.

When implementing the qMT-SIRFSE method, it is very important to keep the predelay time t_d constant, as this was fixed to 3.5s in the original model [13]. If TR is held constant, the analysis model will be more complicated with a third recovery rate component. Figure 3.19 (d) presents an inferior F map from qMT-SIRFSE without fixing t_d.

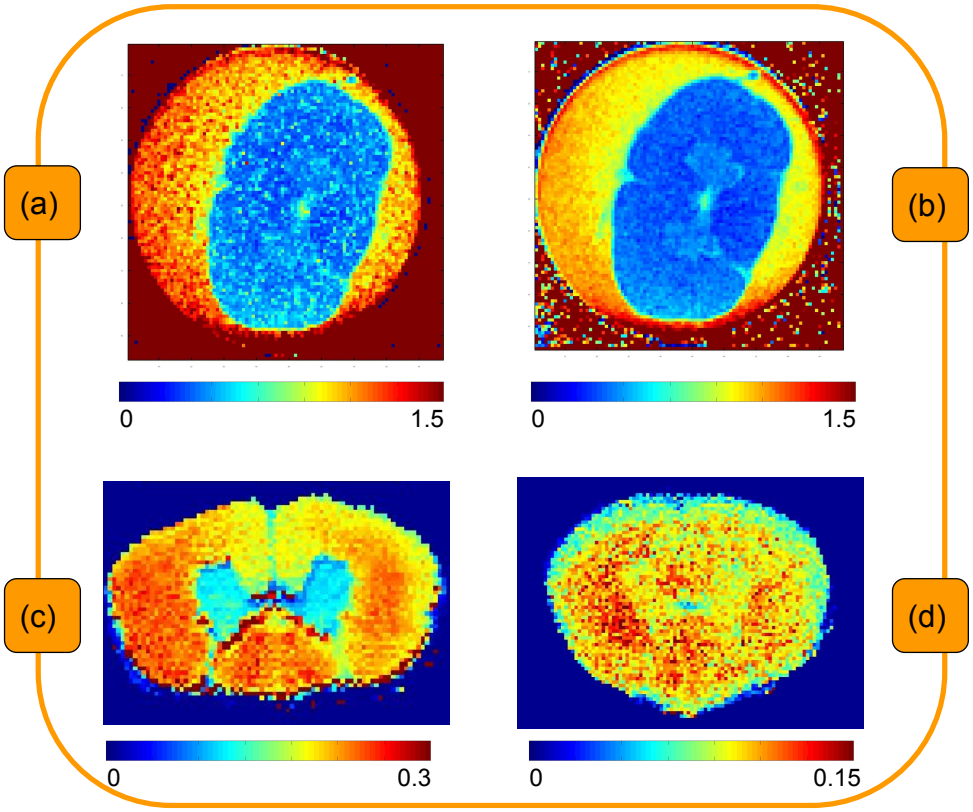

Figure 3.19: Wrong calibration may lead to wrong maps: (a) T_1 map from proton density imaging with incorrect B_1 map and insufficient spoiling, (b) T_1 map from proton density imaging with insufficient spoiling, (c) F from qMT-SPGR with incorrect B_1 map and insufficient spoiling, (d) F from qMT-SIRFSE without fixing delay time t_d.

To standardize the data analysis, qMTLab [20], which was developed by our team, has been upgraded to qMRLab, incorporating diffusion processing and all the myelin imaging techniques implemented in this thesis. In addition, the data of the dog spinal cord [51] are publicly available to help the readers who are interested in reproducing the results of the study conducted for the thesis. The details are listed in Appendix.

3.3.2 Ex vivo spinal cord

All MR techniques exhibit similar trends that are consistent with histology (Figure 3.1, Figure 3.7 and Figure 3.13). The high correlations when including grey matter are primarily due to bulk differences between grey and white matter. In white matter the voxel-wise correlations are significantly lower, both between MR metrics and when compared to histology (Figure 3.2, Figure 3.8 and Figure 3.14). This is not surprising given the lower dynamic range in WM. Moreover, moving the sample between scan sessions may cause certain variance in the scan-rescan results and lead to lower correlations in WM. Previous works has shown lower correlations in WM, between F from qMT-SPGR and MWF [48, 49], F from qMT-SIRFSE and MWF [17], MTV and qMT-SPGR [15]. Mezer et al. [15] showed a moderate correlation (R=0.79) between MTV and MWF, but the study included region-based analysis. It is important to note that temperature and chemical fixation may also affect the intrinsic T_2s and water exchange rates [52-55], and the axon diameter variation across regions may influence intercompartmental water exchange rates [48], therefore these factors can affect qMT and MET2 measurements. Chemical fixation is well known to reduce T_1 and T_2 relaxation times. Birkl et al. [44] showed a reduction in the T_2 relaxation time of 5% and 26% in the thalamus and white matter in a fixed human brain, respectively. Moreover, fixation causes a change in the T_2 relaxation time due to the temperature at which the experiment was conducted. In our study, the bore temperature was around 20^0C while the temperature of in vivo subjects is around 37^0C; therefore, the diffusion coefficient of free water and the intercompartmental water exchange rate are expected to drop significantly. From the results of our work, the observation that the correlations between myelin measures are comparable to the scan-rescan correlations (within measures), suggests that our protocols have similar performance.

With respect to the histological validation, it is important to point out several possible confounding factors: (i) poor compaction of the myelin sheaths which results in imperfect segmentation and overestimation of the MVF values; (ii) high sensitivity to variation of contrast, brightness, and focus (although not visible before downsampling) of the adaptive OTSU segmentation and the automatic segmentation software AxonSeg; (iii) imperfect registration with the MRI-based metrics using the affine transformation.

Some previously published works showed significant correlations between MWF and pool size ratio F with MVF from histology, but the analysis was done in demyelinating or dysmyelinating models where greater variation in absolute myelin content was observed [49] [7, 56-59]. The study in rat spinal cord in [17] also did not find positive correlation between F and MWF with histology by voxel-wise analysis. Low correlation was observed between MTV and histological metrics in a cat spinal cord model [18].

In the rat spinal cord model, the lower correlation observed for F from qMT-SIRSE can be explained by the high sensitivity of the non-linear fitting routines to the Gibbs artifacts which are more pronounced in smaller spinal cords.

While the four myelin imaging techniques exhibit similar specificity to myelin, there are number of factors can be considered when choosing which method to implement. It is up to the scientists to select the most appropriate method depending on their demands. In terms of implementation, proton density imaging may be easiest to implement due to the simplicity of acquisition and the availability of the standard sequences on the scanners. On the other hand, qMT using SIR-FSE sequence needs some customization of the standard fast spin echo sequence. Myelin water imaging requires shorter echo spacing time to take signals from shorter T_2 components into account; and this feature may not always be available on all scanners and may require some sequence customization as well.

The qMT techniques are currently not available as stock sequences on the scanner, so using them requires pulse sequence programming. In terms of data processing, qMT using the SPGR sequence is computationally demanding due to the non-linear fitting and the need for B_1 and B_0 correction. However, the qMT-SPGR method requires shorter scan time and has been extensively tested in vivo, while qMT-SIRFSE requires longer scan times and is not extensively tested in vivo. Recent results from a study by Dortch et al. [39] showed the feasibility of qMT-SIRFSE in human brain in vivo, but multislice imaging is not possible with this approach due to MT effects on neighboring slices caused by the refocusing pulse. Li et al. [40] optimized the protocol by varying both the inversion time (t_i) and the delay time (t_d) qMT-SIRFSE may be a better option in cases of high static/RF inhomogeneities, limited specific absorption rate (SAR) or high susceptibility differences, especially in ultra-high field MRI [39].

There is great promise in multi-modal imaging which combines different methods to distill more information about the white matter microstructure as well as increase the specificity to myelin. Combination of MTR and T_2^* was shown to improve specificity to myelin degeneration in MS [61]. Stikov et al. [62] recently proposed a novel biophysical model which combined magnetization transfer and diffusion imaging to measure the fiber g-ratio, defined as the ratio between the inner and the outer diameter of the white matter fiber, and highlighted its potential for in vivo histology.

CHAPTER 4 CONCLUSION AND RECOMMENDATIONS

4.1 Conclusion

In this work, we implemented and compared several MR-based myelin imaging techniques (quantitative magnetization transfer, proton density imaging, and multi-exponential T_2 imaging) by evaluating their repeatability and their relation to large-scale histology in the ex vivo spinal cords of a rat, a dog, and a human. While there have been studies doing pairwise comparisons and histological validation of the above techniques, to the best of our knowledge this is the first study that implemented and compared all those methods at the same time and looked into their reproducibility and their correlation with absolute myelin content, as measured from electron microscopy.

Qualitatively the contrasts were similar, and all techniques had comparable scan-rescan and correlations with histology. Surprisingly, the voxel-wise correlations between the various myelin measures were almost as high as the scan-rescan correlations. The correlations decreased when only white matter was considered, which could be due to the small dynamic range of the measurement, or due to artifacts related to the preparation and panoramic scanning of the tissue. We conclude that the myelin imaging techniques explored in this thesis exhibit similar specificity to myelin, yet the histological correlations suggest that more work is needed to determine the optimal myelin imaging protocol.

The study also pointed out some potential miscalibrations during acquisitions as well as data processing that may lead to anywhere from minor to major impact on the accuracy of the results. These include B1 mapping, insufficient spoiling and variation of the predelay time. We have also standardized the data processing routines by integrating all data processing routines into the qMRLab toolbox. In addition, the data of the dog spinal cord in this study will be made publicly available to enable easy reproduction of the results presented in this thesis.

4.2 Future work

Standardization is one of the biggest problem our field is facing, and reproducibility is a burning issue. In the absence of a stock myelin imaging protocol available on standard MRI scanners, we recommend that labs collaborate on sharing their protocols and making their data

publicly available. Our lab is taking the first step by making this dataset publicly available, together with the associated processing routines. For more details, please consult the appendix of this thesis.

The protocols need to be adapted to in vivo acquisitions, and their time efficiency should be taken into account when making recommendations. 3D imaging would reduce artifacts and increase SNR for all techniques. If sufficient scan time is available, combining the above techniques should result in greater myelin specificity. Our lab has recently proposed a combined myelin estimation (CME), which uses independent component analysis (ICA) to improve the estimation of myelin content in multiple sclerosis patients [61]. We will explore this approach in healthy white matter and report on the outcome in the near future.

We also plan to increase the statistical power of our study by imaging more spinal cords and performing large-scale histology on the same cohort. The idea is that this study will be used as a jumping board for developing a a statistical framework for analyzing quantitative MRI data. For now, the only conclusions we can draw are about the statistical power of our measurements for the characterization of the specimens at hand. We are currently working with statisticians to formalize this approach and to be able to generalize our findings and to draw conclusions about the precision and accuracy of myelin imaging.

Variations of microstructure between and within species should be taken into account when explaining the differences between the three experiments. In particular, demyelinating models should be included in the analysis, to ensure a wider dynamic range of the MVF measurement. Once we can control the amount of myelin in the specimen, it will be easier to answer the question whether the lower correlations with histology are due to low specificity of the measurements, or due to the small myelin variability within the specimen.

Finally, these studies need to be complemented by more robust large-scale histological techniques that minimize fixation and reconstruction artifacts. Histological acquisition needs to be subjected to a scan-rescan validation to take into account the repeatability of histological metrics. At this moment, we only have the scan-rescan from the MRI protocol, but we cannot be sure whether the histology is truly a gold standard until we can put an upper limit on its reproducibility.

The field of myelin imaging shows great promise, but the questions we are trying to answer are hard. Advances in MR hardware and software will make quantitative imaging routine. Transparency will go a long way toward ensuring that labs can reproduce each other's findings. Multi-modal approaches will enable us to improve our myelin models and to increase myelin specificity; and histology will continue to become more robust and large-scale. To put it all together, we need interdisciplinary research that breaks barriers and builds bridges. Consider this thesis a small bridge across a wide and exciting unknown.

BIBLIOGRAPHY

[1] "Atlas of MS," *Multiple Sclerosis International Federation,* 2013.

[2] I. I. Rabi, J. M. B. Kellogg, and J. R. Zacharias, "The Magnetic Moment of the Proton," *Physical Review,* vol. 46, pp. 157-163, 08/01/ 1934.

[3] I. I. Rabi, J. M. B. Kellogg, and J. R. Zacharias, "The Magnetic Moment of the Deuton," *Physical Review,* vol. 46, pp. 163-165, 08/01/ 1934.

[4] I. I. Rabi, J. R. Zacharias, S. Millman, and P. Kusch, "A New Method of Measuring Nuclear Magnetic Moment," *Physical Review,* vol. 53, pp. 318-318, 02/15/ 1938.

[5] D. G. Nishimura, "Principles of magnetic resonance imaging," *Department of Electrical Engineering, Stanford University,* 2010.

[6] N. Stikov, "Quantitative magnetic resonance imaging of the macromolecular proton pool in tissue," *Ph.D thesis, Stanford University,* 2009.

[7] C. Laule, E. Leung, D. K. Li, A. L. Traboulsee, D. W. Paty, A. L. MacKay*, et al.*, "Myelin water imaging in multiple sclerosis: quantitative correlations with histopathology," *Multiple Sclerosis,* vol. 12, pp. 747-753, 2006.

[8] C. Laule, I. M. Vavasour, S. H. Kolind, D. K. B. LI, T. L. Traboulsee, G. R. Moore*, et al.*, "Magnetic resonance imaging of myelin," *Neurotherapeutics,* vol. 4, July 2007.

[9] A. Waldman, J. H. Rees, C. S. Brock, M. D. Robson, P. D. Gatehouse, and G. M. Bydder, "MRI of the brain with ultra-short echo-time pulse sequences," *Neuroradiology,* vol. 45, pp. 887-892, Dec 2003.

[10] M. J. Wilhelm, H. H. Ong, S. L. Wehrli, C. Li, P. H. Tsai, D. B. Hackney*, et al.*, "Direct magnetic resonance detection of myelin and prospects for quantitative imaging of myelin density," *Proceedings of the National Academy of Sciences of the United States of America,* vol. 109, pp. 9605-9610, Jun 2012.

[11] J. Cohen-Adad and C. Wheeler-Kingshott, "Quantitative MRI of the spinal cord," *Academic Press,* 2014.

[12] J. G. Sled and G. B. Pike, "Quantitative interpretation of magnetization transfer in spoiled gradient echo MRI sequences," *Journal of Magnetic Resonance,* vol. 145, pp. 24-36, Jul 2000.

[13] D. F. Gochberg and J. C. Gore, "Quantitative magnetization transfer imaging via selective inversion recovery with short repetition times," *Magn Reson Med,* vol. 57, pp. 437-41, Feb 2007.

[14] A. Mackay, K. Whittall, J. Adler, D. Li, D. Paty, and D. Graeb, "In-vivo visualization of myelin water in brain by magnetic-resonance," *Magnetic Resonance in Medicine,* vol. 31, pp. 673-677, Jun 1994.

[15] A. Mezer, J. D. Yeatman, N. Stikov, K. N. Kay, N. J. Cho, R. F. Dougherty*, et al.*, "Quantifying the local tissue volume and composition in individual brains with magnetic resonance imaging," *Nat Med,* vol. 19, pp. 1667-72, Dec 2013.

[16] J. G. Sled and G. B. Pike, "Quantitative interpretation of magnetization transfer in spoiled gradient echo MRI sequences," *J Magn Reson,* vol. 145, pp. 24-36, Jul 2000.

[17] A. N. Dula, D. F. Gochberg, H. L. Valentine, W. M. Valentine, and M. D. Does, "Multiexponential T2, magnetization transfer, and quantitative histology in white matter tracts of rat spinal cord," *Magn Reson Med,* vol. 63, pp. 902-9, Apr 2010.

[18] T. Duval, B. Perraud, M.-T. Vuong, N.-L. Rios, N. Stikov, and J. Cohen-Adad, "Validation of quantitative MRI metrics using full slice histology with automatic axon segmentation," *Proceedings of the 24th Annual Meeting of ISMRM,* 2016.

[19] S. G. Waxman and M. V. Bennett, "Relative conduction velocities of small myelinated and non-myelinated fibres in the central nervous system," *Nat New Biol,* vol. 238, pp. 217-9, 1972.

[20] J.-F. Cabana, Y. Gu, M. Boudreau, I. R. Levesque, Y. Atchia, J. G. Sled*, et al.*, "Quantitative magnetization transfer imagingmadeeasy withqMTLab: Software for data simulation, analysis, and visualization," *Concepts in Magnetic Resonance Part A,* vol. 44A, pp. 263-277, 2015.

[21] E. K. Insko and L. Bolinger, "Mapping of the radiofrequency field," *Journal of Magnetic Resonance Series A,* vol. 103, pp. 82-85, Jun 1993.

[22] V. L. Yarnykh, "Actual flip-angle imaging in the pulsed steady state: a method for rapid three-dimensional mapping of the transmitted radiofrequency field," *Magn Reson Med,* vol. 57, pp. 192-200, Jan 2007.

[23] L. I. Sacolick, F. Wiesinger, I. Hancu, and M. W. Vogell, "B-1 Mapping by Bloch-Siegert Shift," *Magnetic Resonance in Medicine,* vol. 63, pp. 1315-1322, May 2010.

[24] J. K. Barral, E. Gudmundson, N. Stikov, M. Etezadi-Amoli, P. Stoica, and D. G. Nishimura, "A Robust Methodology for In Vivo T-1 Mapping," *Magnetic Resonance in Medicine,* vol. 64, pp. 1057-1067, Oct 2010.

[25] N. Stikov, M. Boudreau, I. R. Levesque, C. L. Tardif, J. K. Barral, and G. B. Pike, "On the Accuracy of T-1 Mapping: Searching for Common Ground," *Magnetic Resonance in Medicine,* vol. 73, pp. 514-522, Feb 2015.

[26] H. L. Cheng, N. Stikov, N. R. Ghugre, and G. A. Wright, "Practical medical applications of quantitative MR relaxometry," *J Magn Reson Imaging,* vol. 36, pp. 805-24, Oct 2012.

[27] T. Duval, S. Le Vy, N. Stikov, J. Campbell, A. Mezer, T. Witzel*, et al.*, "g-Ratio weighted imaging of the human spinal cord in vivo," *Neuroimage,* vol. 145, pp. 11-23, Jan 15 2017.

[28] E. Alonso-Ortiz, I. R. Levesque, and G. B. Pike, "MRI-Based Myelin Water Imaging: A Technical Review," *Magnetic Resonance in Medicine,* vol. 73, pp. 70-81, Jan 2015.

[29] L. Vidarsson, S. M. Conolly, K. O. Lim, G. E. Gold, and J. M. Pauly, "Echo time optimization for linear combination myelin Imaging," *Magnetic Resonance in Medicine,* vol. 53, pp. 398-407, Feb 2005.

[30] R. M. Henkelman, G. J. Stanisz, and S. J. Graham, "Magnetization transfer in MRI: a review," *Nmr in Biomedicine,* vol. 14, pp. 57-64, Apr 2001.

[31] P. J. Gareau, B. K. Rutt, S. J. Karlik, and J. R. Mitchell, "Magnetization transfer and multicomponent T2 relaxation measurements with histopathologic correlation in an experimental model of MS," *Journal of Magnetic Resonance Imaging,* vol. 11, pp. 586-595, Jun 2000.

[32] R. M. Henkelman, X. Huang, Q. S. Xiang, G. J. Stanisz, S. D. Swanson, and B. M. J., "Quantitative interpretation of magnetization transfer," *Magn Reson Med,* vol. 29, pp. 759-766, 1993.

[33] S. J. Graham and R. M. Henkelman, "Understanding pulsed magnetization transfer," *Jmri-Journal of Magnetic Resonance Imaging,* vol. 7, pp. 903-912, Sep-Oct 1997.

[34] P. Mossahebi, "Quantitative magnetization transfer imaging: theory and applications," *PhD thesis, University of Wisconsin-Madison,* 2013.

[35] A. Ramani, C. Dalton, D. H. Miller, P. S. Tofts, and G. J. Barker, "Precise estimate of fundamental in-vivo MT parameters in human brain in clinically feasible times," *Magnetic Resonance Imaging,* vol. 20, pp. 721-731, Dec 2002.

[36] E. Schneider and G. Glover, "RAPID INVIVO PROTON SHIMMING," *Magnetic Resonance in Medicine,* vol. 18, pp. 335-347, Apr 1991.

[37] J. G. Sled and G. B. Pike, "Quantitative imaging of magnetization transfer exchange and relaxation properties In vivo using MRI," *Magn Reson Med,* vol. 46, pp. 923-931, 2001.

[38] G. B. Pike, "Pulsed magnetization transfer contrast in gradient echo imaging: A two-pool analytic description of signal response," *Magnetic Resonance in Medicine,* vol. 36, pp. 95-103, Jul 1996.

[39] R. D. Dortch, K. Li, D. F. Gochberg, E. B. Welch, A. N. Dula, A. A. Tamhane*, et al.*, "Quantitative Magnetization Transfer Imaging in Human Brain at 3 T via Selective Inversion Recovery," *Magnetic Resonance in Medicine,* vol. 66, pp. 1346-1352, Nov 2011.

[40] K. Li, Z. Zu, J. Xu, V. A. Janve, J. C. Gore, M. D. Does*, et al.*, "Optimized inversion recovery sequences for quantitative T1 and magnetization transfer imaging," *Magn Reson Med,* vol. 64, pp. 491-500, Aug 2010.

[41] S. Mikula and W. Denk, "High-resolution whole-brain staining for electron microscopic circuit reconstruction," *Nat Meth,* vol. 12, pp. 541-546, 06//print 2015.

[42] H. L. More, J. Chen, E. Gibson, J. M. Donelan, and M. F. Beg, "A semi-automated method for identifying and measuring myelinated nerve fibers in scanning electron microscope images," *Journal of Neuroscience Methods,* vol. 201, pp. 149-158, 2011/09/30/ 2011.

[43] G. Knott, H. Marchman, D. Wall, and B. Lich, "Serial Section Scanning Electron Microscopy of Adult Brain Tissue Using Focused Ion Beam Milling," *The Journal of Neuroscience,* vol. 28, pp. 2959-2964, 2008.

[44] C. Birkl, C. Langkammer, N. Golob-Schwarzl, M. Leoni, J. Haybaeck, W. Goessler*, et al.*, "Effects of formalin fixation and temperature on MR relaxation times in the human brain," *NMR in Biomedicine,* vol. 29, pp. 458-465, 2016.

[45] E. Kellner, B. Dhital, V. G. Kiselev, and M. Reisert, "Gibbs-ringing artifact removal based on local subvoxel-shifts," *Magnetic Resonance in Medicine,* vol. 76, pp. 1574-1581, 2016.

[46] N. Otsu, "A threshold selection method from gray level histograms," *IEEE Trans. Syst. Man Cybern.,* vol. SMC-9, pp. 62 -66, 1979.

[47] A. Zaimi, T. Duval, A. Gasecka, D. Cote, N. Stikov, and J. Cohen-Adad, "AxonSeg: Open Source Software for Axon and Myelin Segmentation and Morphometric Analysis," *Frontiers in Neuroinformatics,* vol. 10, Aug 2016.

[48] J. G. Sled, I. Levesque, A. C. Santos, S. J. Francis, S. Narayanan, S. D. Brass*, et al.*, "Regional variations in normal brain shown by quantitative magnetization transfer imaging," *Magn Reson Med,* vol. 51, pp. 299-303, Feb 2004.

[49] D. J. Tozer, G. R. Davies, D. R. Altmann, D. H. Miller, and P. S. Tofts, "Correlation of apparent myelin measures obtained in multiple sclerosis patients and controls from magnetization transfer and multicompartmental T2 analysis," *Magnetic Resonance in Medicine,* vol. 53, pp. 1415-1422, 2005.

[50] K. D. Harkins and M. D. Does, "Simulations on the influence of myelin water in diffusion-weighted imaging," *Physics in Medicine and Biology,* vol. 61, pp. 4729-4745, Jul 7 2016.

[51] M.-T. Vuong, T. Duval, J. Cohen-Adad, and N. Stikov, "On the Precision of Myelin Imaging: Characterizing Ex vivo Dog Spinal Cord with MRI and Histology," *Proceedings of the 25th Annual Meeting of ISMRM,* 2017.

[52] T. A. Bjarnason, I. M. Vavasour, C. L. L. Chia, and A. L. MacKay, "Characterization of the NMR behavior of white matter in bovine brain," *Magnetic Resonance in Medicine,* vol. 54, pp. 1072-1081, 2005.

[53] P. Kozlowski, J. Liu, A. C. Yung, and W. Tetzlaff, "High-resolution myelin water measurements in rat spinal cord," *Magnetic Resonance in Medicine,* vol. 59, pp. 796-802, 2008.

[54] T. M. Shepherd, P. E. Thelwall, G. J. Stanisz, and S. J. Blackband, "Aldehyde fixative solutions alter the water relaxation and diffusion properties of nervous tissue," *Magnetic Resonance in Medicine,* vol. 62, pp. 26-34, 2009.

[55] H. E. D'Arceuil, S. Westmoreland, and A. J. de Crespigny, "An approach to high resolution diffusion tensor imaging in fixed primate brain," *NeuroImage,* vol. 35, pp. 553-565, 4/1/ 2007.

[56] K. Schmierer, D. J. Tozer, F. Scaravilli, D. R. Altmann, G. J. Barker, P. S. Tofts*, et al.*, "Quantitative magnetization transfer imaging in postmortem multiple sclerosis brain," *Journal of Magnetic Resonance Imaging,* vol. 26, pp. 41-51, 2007.

[57] K. Schmierer, C. A. M. Wheeler-Kingshott, D. J. Tozer, P. A. Boulby, H. G. Parkes, T. A. Yousry*, et al.*, "Quantitative magnetic resonance of postmortem multiple sclerosis brain before and after fixation," *Magnetic Resonance in Medicine,* vol. 59, pp. 268-277, 2008.

[58] S. Webb, C. A. Munro, R. Midha, and G. J. Stanisz, "Is multicomponent T2 a good measure of myelin content in peripheral nerve?," *Magnetic Resonance in Medicine,* vol. 49, pp. 638-645, 2003.

[59] G. J. Stanisz, S. Webb, C. A. Munro, T. Pun, and R. Midha, "MR properties of excised neural tissue following experimentally induced inflammation," *Magnetic Resonance in Medicine,* vol. 51, pp. 473-479, 2004.

[60] I. R. Levesque and G. B. Pike, "Characterizing healthy and diseased white matter using quantitative magnetization transfer and multicomponent T2 relaxometry: A unified view via a four-pool model," *Magnetic Resonance in Medicine,* vol. 62, pp. 1487-1496, 2009.

[61] G. Mangeat, S. T. Govindarajan, C. Mainero, and J. Cohen-Adad, "Multivariate combination of magnetization transfer, T2* and B0 orientation to study the myelo-architecture of the in vivo human cortex," *Neuroimage,* vol. 119, pp. 89-102, Oct 1 2015.

[62] N. Stikov, J. S. Campbell, T. Stroh, M. Lavelee, S. Frey, J. Novek*, et al.*, "In vivo histology of the myelin g-ratio with magnetic resonance imaging," *Neuroimage,* vol. 118, pp. 397-405, Sep 2015.

APPENDIX A – DOCUMENTATION

To standardize the data analysis, qMTLab [20], which was developed by our team, has been upgraded to qMRLab to incorporate diffusion imaging and all of the myelin imaging techniques used in this thesis. In addition, the data of the dog spinal cord [51] are published to help the readers who are interested in reproducing the results of all the methods. The data and analysis scripts can be viewed at the following address, using the experimental Jupyter Binder platform. The analysis below is courtesy of Agah Karakuzu:

http://beta.mybinder.org/v2/gh/agahkarakuzu/dogSC/a663416909b469d7f9c08acaf7d0dcfc02e1f3ac?filepath=dogSC.ipynb

The open source software qMRLab is available at the following address:

https://github.com/neuropoly/qMRLab

The readers can find the updated documentation in the guideline document ReadMe.docx published at the same address.

1. Preprocessing

Gibbs correction: the Gibbs ringing artifact is reduced by using the unring tool published at https://bitbucket.org/reisert/unring based on the algorithm described in [45].

2. Data tree

The following data tree summarizes the data input for each method using qMRLab.

2.1. qMT-SIRFSE

- MTdata.nii/.mat
- R1map.nii/.mat
- Protocol.mat (TI)

2.2. qMT-SPGR

- MTdata.nii/.mat
- R1map.nii/.mat
- B1map.nii/.mat
- B0map.nii/.mat
- Protocol.mat (Angles, Offset)

2.3. Proton density imaging (MTV)

- SPGRdata.nii/.mat

- B1map.nii/.mat
- T1map.nii/.mat
- CSFmask.nii/.mat
- Protocol.mat (flipAngles,TR)

2.4. Multi-exponential T_2 imaging (MWF)

- MET2data.nii
- Protocol.mat

2.5. Field Maps

- B1_DAM (Double-Angle Method)
  - SF60.nii (spin echo with a flip angle of 60)
  - SF120.nii (spin echo with a flip angle of 120)

- B0_DualEcho
  - Phase.nii
  - Magn.nii
  - Protocol.mat (ESP2)

3. Generate Parameters.mat

Open qMRILab with the *Command Window*

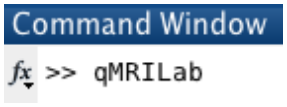

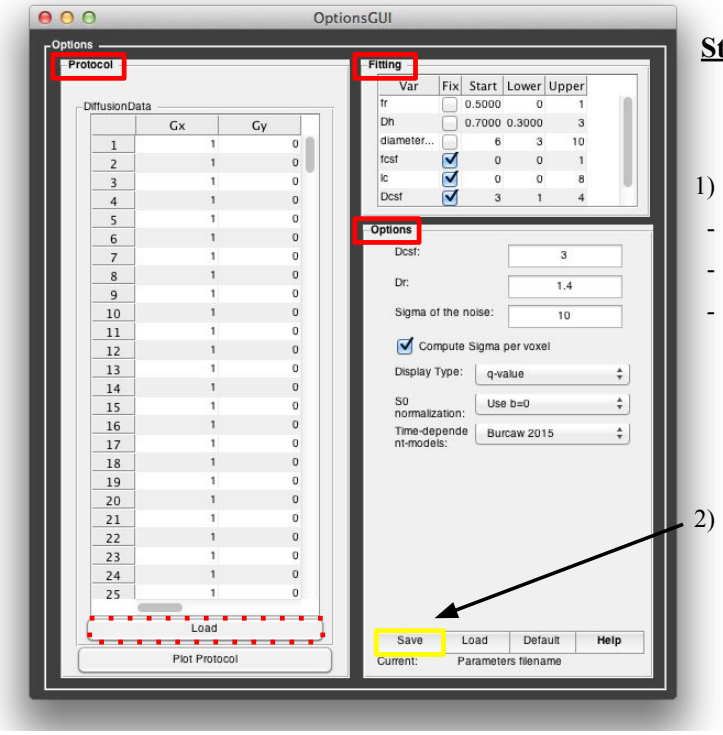

Steps:

1) Fill:
- *Protocol* (* You can also load it *)
- *Fitting*
- *Options*

2) Save all those parameters to generate the file *Parameters.mat*

4. Scripting

While data can be fitted using the graphical user interface (GUI) of qMRLab, users who are familiar with scripting can use fitting functions directly on the console of MATLAB and that can be helpful when they want to process their data in an automatic manner.

```
%% 4.1 - Load dataset

% Load your parameters to create your Model
% load('Parameters.mat')
load('qMRILab_CHARMEDParameters.mat');

% Create a struct "file" that contains the NAME of all data's FILES
% file.DATA = 'FILE_NAME'
file.DiffusionData = 'DiffusionData.nii.gz';
file.Mask = 'Mask.nii.gz';


%% 4.2 - Check data and fitting (Optional)

qMRILab(Model,file);
```

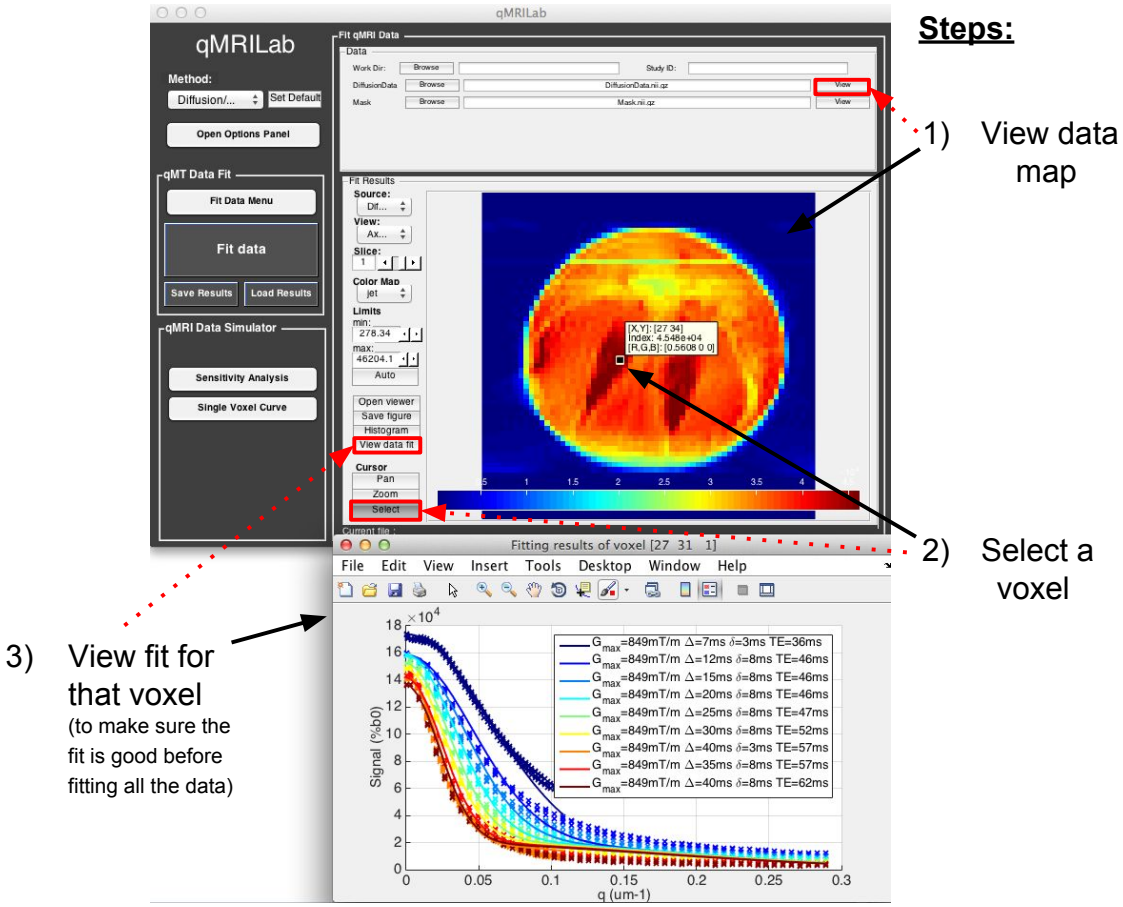


```
%% 4.3 - Create Quantitative Maps

% Create a struct "data" that contains all the data
% data.DATA = load_nii_data('FILE_NAME')
data.DiffusionData = load_nii_data('DiffusionData.nii.gz');
data.Mask = load_nii_data('Mask.nii.gz');

% Fit your data
FitResults = FitDataCustom(Model,data);

% Save your results
% FitResulsSave_nii(FitResults, fname_copyheader,folder)
FitResultsSave_nii(FitResults,'DiffusionData.nii.gz','FitResults');
```

5. Data processing pipelines

5.1. Fitting

The fitting procedures were described above and are further explained in the instruction file after downloading the qMRLab software. Readers can also read the wiki of qMRLab at the following address:
https://github.com/neuropoly/qMRLab/wiki

5.2. Create Mask

Depending on the regions of interest, appropriate masks need to be created for fitting and statistics.

5.3. Registration

To register histological metrics to MRI-based metrics or to perform scan-rescan registration, one can use the available tools from the automatic segmentation open software AxonSeg [47].

5.4. Compute statistics

Voxel-wise correlations can be easily computed using the available function in MATLAB. The following example shows how to calculate Pearson's correlation between MWF and MTV in a region of interest defined by a mask.

```
x=mwf(mask); %MWF data in a region of interest defined by a mask.
y=mtv(mask); %MTV data in a region of interest defined by a mask
plot(x,y,'+'); % scatter plots of MWF and MTV
corr(x,y); %  calculate Pearson's correlation between MWF and MTV.
```